

UC Riverside

UC Riverside Electronic Theses and Dissertations

Title

Inch-Scale High Throughput Metrology of Graphene and Patterned Graphene Oxide

Permalink

<https://escholarship.org/uc/item/6ph5z87m>

Author

Pleskot, Dennis

Publication Date

2013

Peer reviewed|Thesis/dissertation

UNIVERSITY OF CALIFORNIA
RIVERSIDE

Inch-Scale High Throughput Metrology of Graphene
and Patterned Graphene Oxide

A Thesis submitted in partial satisfaction
of the requirements for the degree of

Master of Science

in

Materials Science and Engineering

by

Dennis L Pleskot

June 2013

Thesis Committee:

Dr. Cengiz Ozkan, Chairperson

Dr. Kambiz Vafai

Dr. Sandeep Kumar

Dr. Mihri Ozkan

Copyright by
Dennis L Pleskot
2013

The Thesis of Dennis L Pleskot is approved:

Committee Chairperson

University of California, Riverside

Acknowledgements

I would like to thank Dr. Jennifer Kyle for her substantial help in this project, particularly with regard to the development of the image processing software. I would also like to recognize Dr. Maziar Ghazinejad and Dr. David Carter for their helpful advice on the details of fluorescence imaging. I am also grateful for the contributions made by Jeffrey Bell, Zafer Mutlu, and Isaac Ruiz. Lastly, I want to thank Drs. Cengiz and Mihri Ozkan for their guidance over this project and their stewardship over my graduate studies for the past two and half years. Much of the original work of this study has been published in Nanotechnology Communications.

ABSTRACT OF THE THESIS

Inch-Scale High Throughput Metrology of Graphene and Patterned Graphene Oxide

by

Dennis L Pleskot

Master of Science, Graduate Program in Materials Science and Engineering
University of California, Riverside, June 2013
Dr. Cengiz Ozkan, Chairperson

In order to fully utilize the unique properties of graphene, large-area sheets of the material must be produced. As the demand for large, continuous sheets of graphene increases, the need to quickly and effectively characterize such a material correspondingly increases. In tandem, the use of patterned graphene oxide in practical applications has also expanded at a rapid pace, leading to a greater need to characterize this material as well. In this study, fluorescence quenching microscopy was examined as a means of analyzing 4 in² sheets of graphene and patterned graphene oxide in a fast and efficient manner. It was determined that fluorescence microscopy offers a number of advantages in imaging these materials over conventional techniques such as Raman spectroscopy, SEM, and TEM. Fluorescence microscopy proved to be a highly scalable technique that is able to image a graphitic material in substantially less time than would be possible in these other methods while still maintaining adequate resolution. Unlike SEM and TEM, fluorescence microscopy is also a non-destructive characterization technique, allowing the samples that were actually characterized to be used in practical applications. Additionally, a clear contrast between graphene oxide and pristine graphene could be observed. Analysis of the fluorescence contrast histogram shows that graphene oxide

displays a unique intensity peak and can thus not only be distinguished from pristine graphene but also defects in the sample, the presence of multiple layers, and changes in the uniformity of the graphene surface. These observations and results demonstrate the expanding usefulness of fluorescence microscopy as a high-throughput characterization technique.

Table of Contents

Chapter 1: Background on Graphene and Graphene Oxide	1
Chapter 2: Current Characterization Techniques	4
Chapter 3: Applications of Large-Area Graphene and Graphene Oxide.....	19
Chapter 4: Background and Motivation for Fluorescence Microscopy	21
Chapter 5: Theory of FRET	34
Chapter 6: Experimental Procedures	36
Chapter 7: Observations and Results.....	42
Conclusion.....	49
References	50
Appendix: Image Processing Software.....	54

List of Figures

Figure 1 Single-Layer Graphene Sheet.....	1
Figure 2 Graphene Oxide Structure	2
Figure 3 Raman Spectrometer	4
Figure 4 Raman Spectroscopy of Graphene	5
Figure 5 Raman Spectra for Several Possible Graphene Oxide Structures.....	8
Figure 6 SEM Apparatus.....	10
Figure 7 SEM of CVD-Grown Graphene on Copper Substrates	12
Figure 8 SEM of Graphene Oxide Flakes on Si Wafers.....	14
Figure 9 TEM Apparatus.....	15
Figure 10 TEM of Tobacco Mosaic Virus (TMV) Supported by Graphene Sheets.....	16
Figure 11 TEM of Graphene Oxide.....	17
Figure 12 Schematic of a Fluorescence Microscope.....	21
Figure 13 Fluorescence Microscopy of Biological Cells.....	23
Figure 14 Comparison of Fluorescence Microscopy and FDG-PET in Determining Cancer Drug Effectiveness	24
Figure 15 Fluorescence of Glucose in Pancreatic Beta Cells.....	26
Figure 16 Viability of Cells with Fluorescent Markers	28
Figure 17 Fluorescence Microscopy of Oxidative Stress Products	29
Figure 18 Comparison of Fluorescence Microscopy with CellROX Deep Red.....	29
Figure 19 FQM of Centimeter-Scale Graphene.....	31
Figure 20 FQM of Doped Graphene.....	32
Figure 21 Schematic of a Typical CVD Tube Furnace for Graphene Growth	36
Figure 22 Schematic of the Fluorescence Imaging Technique.....	39
Figure 23 Fluorescence Image of 2 x 2 in Graphene.....	42
Figure 24 Raman Spectra of Large-Area Graphene Before and After Fluorescence Imaging.	43
Figure 25 Fluorescent Image of Patterned Graphene Oxide	44
Figure 26 Raman Analysis of Patterned Graphene Oxide.....	47

List of Tables

Table 1 Mean Contrast Values for Pristine Graphene and GO.....45

Chapter 1: Background on Graphene and Graphene Oxide

Graphene has proven to be a highly significant material since its discovery in 2004 by A.K Geim and K.S Novosolov. Graphene was first isolated through micromechanical cleavage, which involved removing layers of graphene from bulk graphite using common Scotch tape, and then transferring it to a thin SiO₂-coated Si wafer. Analysis from optical microscopy later revealed the presence of single-layer graphene produced by this technique¹. As described in their publication, graphene is a two-dimensional monolayer of graphite consisting of hexagonally arranged carbon atoms, as shown in Figure 1.

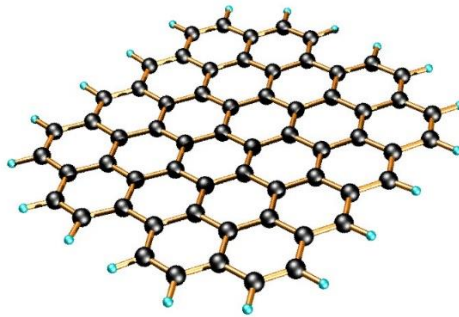


Figure 1 Single-Layer Graphene Sheet²

The carbon atoms are bound together in sp² hybridized orbitals, allowing for unbound pi-orbitals to exist orthogonal to the graphene plane. Graphene displays numerous unique and beneficial properties, such as being over 100 times stronger than steel³, making it one of the strongest materials currently known to exist. Other notable mechanical properties include a high breaking strength of 42 N/m and an elastic stiffness of 340 N/m⁴. Graphene also demonstrates

electron and hole mobilities⁵ of $15,000 \text{ cm}^2\text{V}^{-1}\text{s}^{-1}$ and thermal conductivity⁶ of 5000 KWmK^{-1} .

Electrons in graphene also display zero effective rest mass, causing it to behave as a zero band-gap semiconductor⁷.

Similar to graphene, graphene oxide (GO) also forms two-dimensional sheet-like structures. The structure of graphene oxide is shown in Figure 2. Graphene oxide is

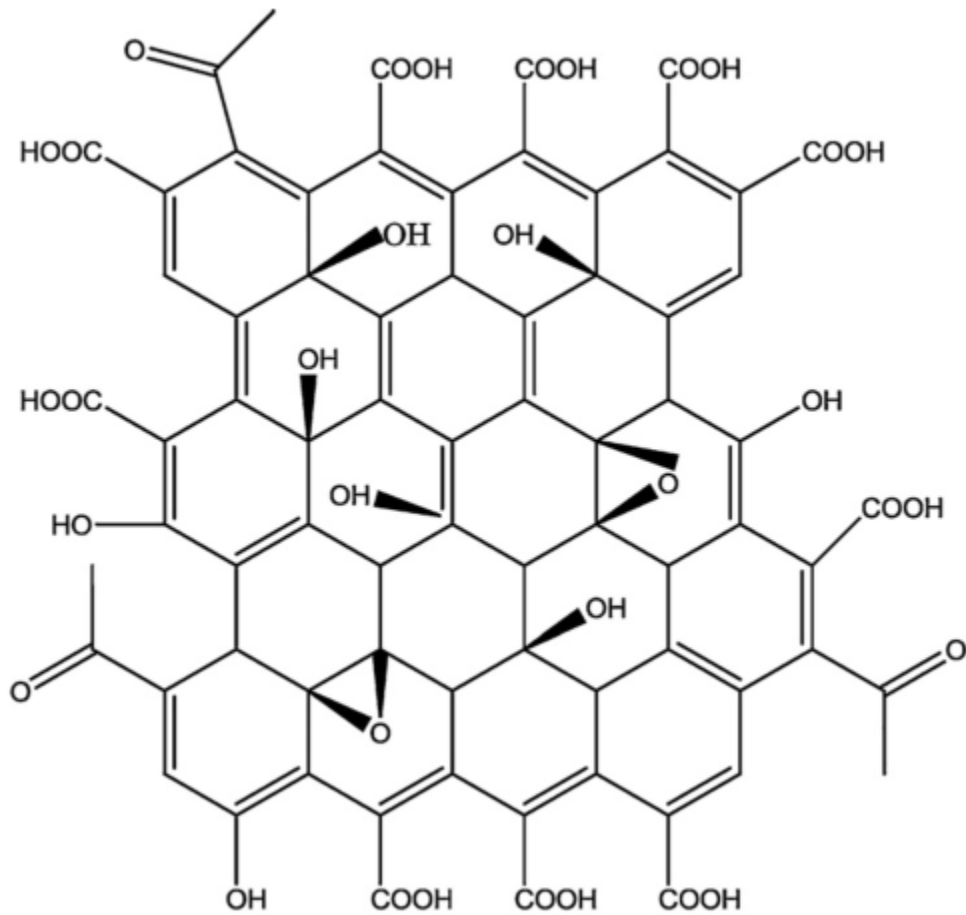


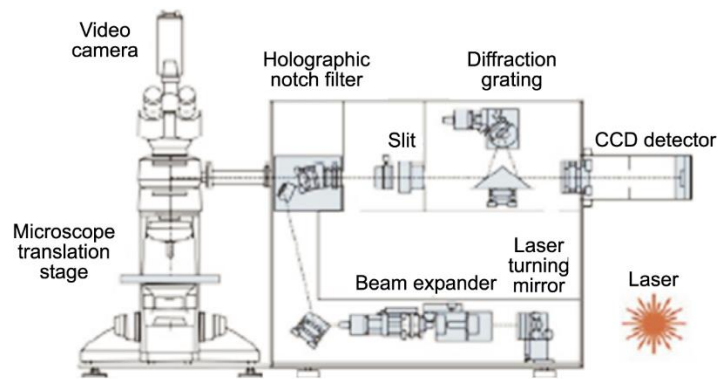
Figure 2 Graphene Oxide Structure⁸

generally manufactured through a top-down approach that involves placing carbon nanotubes in a solution of H_2SO_4 and KMnO_4 . The solution then cuts the nanotubes into long nanoribbon

sheets and coats the surface of these sheets with O or OH groups⁹. Whereas graphene consists of a continuous sp^2 hybridized structure, the bonding of carbon with oxygen atoms causes graphene oxide to display sp^3 hybridization.

Chapter 2: Current Characterization Techniques

Common characterization techniques of nanoscale thin-film materials include Raman spectroscopy, scanning electron microscopy (SEM), and transmission electron microscopy (TEM). Raman microscopy generally works by detecting inelastic scattering of laser light as it interacts with the atomic structure of materials. A schematic of a Raman spectrometer is given in Figure 3.



Source: Smith G. D. *et al.* (2004). With permission

Figure 3 Raman Spectrometer

As seen in the figure, a laser provides the light source, which then passes through a series of filters and mirrors until it interacts with the sample. As incoming light interacts with the sample, constituent elements absorb energy from or transmit energy to the incident beam, causing the transmitted beam to exhibit either a higher wavelength than the incident beam, known as a Stokes shift, or a lower wavelength than the incident beam, known as an Anti-Stokes shift. The transmitted light is then collected at a CCD detector.

Raman spectroscopy displays numerous advantages as a characterization technique, such as being able to accurately identify the composition of a wide range of samples in bulk,

thin-film, and powder form. Also, Raman spectroscopy is a non-destructive process since it uses relatively low-energy laser light to image materials. However, this method is only able to image very small areas at a time, leading to long imaging times, often up to several days to image a 1 in x 1 in sample.

Characterization of graphene through Raman spectroscopy has been extensively documented in literature. In particular, one recent study gives a detailed overview of the process of Raman spectroscopy in graphene¹⁰. Their work can be summarized below in Figure 4.

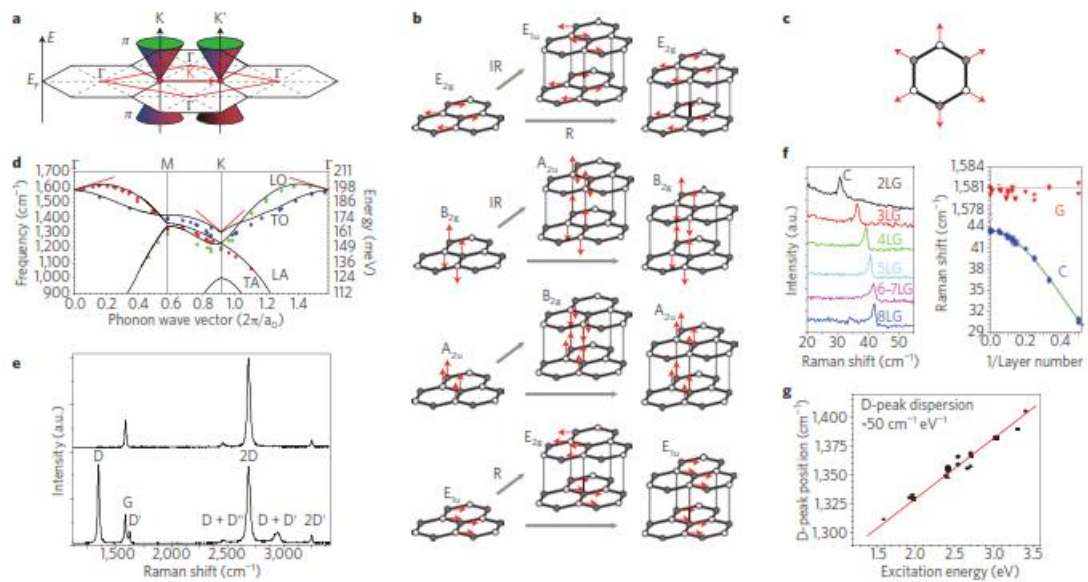


Figure 4 Raman Spectroscopy of Graphene

In order to understand Raman spectroscopy of graphene, it is essential for one to comprehend the phonon distribution present in this material. Figure 4a depicts the Brillouin zones in graphene, with the black hexagons labelled Γ identifying the electronic Brillouin zones, the red tetrahedron displaying the first-phonon Brillouin zones, and the cones labelled K and K'

representing the regions of electronic (Dirac) dispersion. Phonon modes can be associated with different Brillouin zones in a material and can be classified as either acoustic (A) or optical (O) in nature and as longitudinal (L), transverse (T), or out-of-plane (Z) in direction. A plot of the different energies versus wave vector for the in-plane phonon modes is given in Figure 4d. The structure of single-layer graphene contains two atoms per unit cell, leading to a total of six phonon modes centered at the Γ centers. These phonon modes are denoted by A_{2u} , E_{1u} , B_{2g} , and E_{2g} . The modes B_{2g} and E_{2g} are doubly degenerate modes and symbolize the out-of-plane optical modes and in-plane optical modes, respectively.

Figure 4b depicts the four non-degenerate phonon modes present in graphene along with their corresponding modes in graphite. As shown in the figure, for each phonon mode in graphene, there are two modes in graphite, which is due to the fact that graphite contains four atoms per unit cell as opposed to two atoms for graphene. The red arrows in the diagram represent atom displacements for each of the modes shown. Modes E_{2g} and B_{2g} are infrared active (IR) whereas E_{1u} is Raman active (R). Along with these four modes, graphene also displays additional modes located at other Brillouin centers. Figure 4c shows the atom displacements for the A_{1g} mode centered at K. Raman spectroscopy of graphene generally yields three major distinct peaks that correspond to phonon modes located at different Brillouin centers. The characteristic G peak of graphene results from the E_{2g} phonon modes located at Γ centers. The D peak, however, arises from transverse optical (TO) phonons located at K and requires a defect for activation. Along with this, the G' or 2D peak can be described as the second order overtones of the D peak.

Typical Raman spectra for graphene are given in Figure 4e, with the top spectrum depicting pristine graphene and the bottom one representing defective graphene. Because the phonons that generate the D peak require defects to become activated, the D peak is absent from the spectrum of the pristine sample, leaving only the characteristic G and 2D peaks. In contrast, the defective graphene spectrum displays a very large D peak, as well as several other smaller peaks that are the results of the interactions between phonons that generate the D peak and other phonons in the material. Also, the study shows that Raman peaks shift depending on the number of graphene layers present. Graphite contains a C peak resulting from low-frequency E_{2g} phonon modes and is generally linked to interlayer coupling interactions. Figure 4f demonstrates how this peak increasingly shifts position in the spectrum as the number of graphene layers decreases. Also, the graphene D peak tends to shift according to the amount of excitation energy, as depicted in Figure 4g.

In addition to pristine graphene, graphene oxide has also been widely characterized by Raman spectroscopy in literature. In particular, one study conducted extensive modelling of graphene oxide structure¹¹. Several potential models for the distribution of the oxygen atoms on the graphene surface were devised and corresponding Raman spectra were determined for each potential structure. Figure 5 shows a schematic of these graphene oxide structures along with the Raman data. The five hypothesized structures of graphene oxide are depicted in Figures a – e. In these figures, the red atoms represent oxygen whereas the smaller white atoms represent the main carbon lattice of the underlying graphene. Figure 5a shows the Scholz-Boehm model for graphene oxide, referred to as R1, which consists of interlacing graphene ribbons with single-atom rows of oxygen.

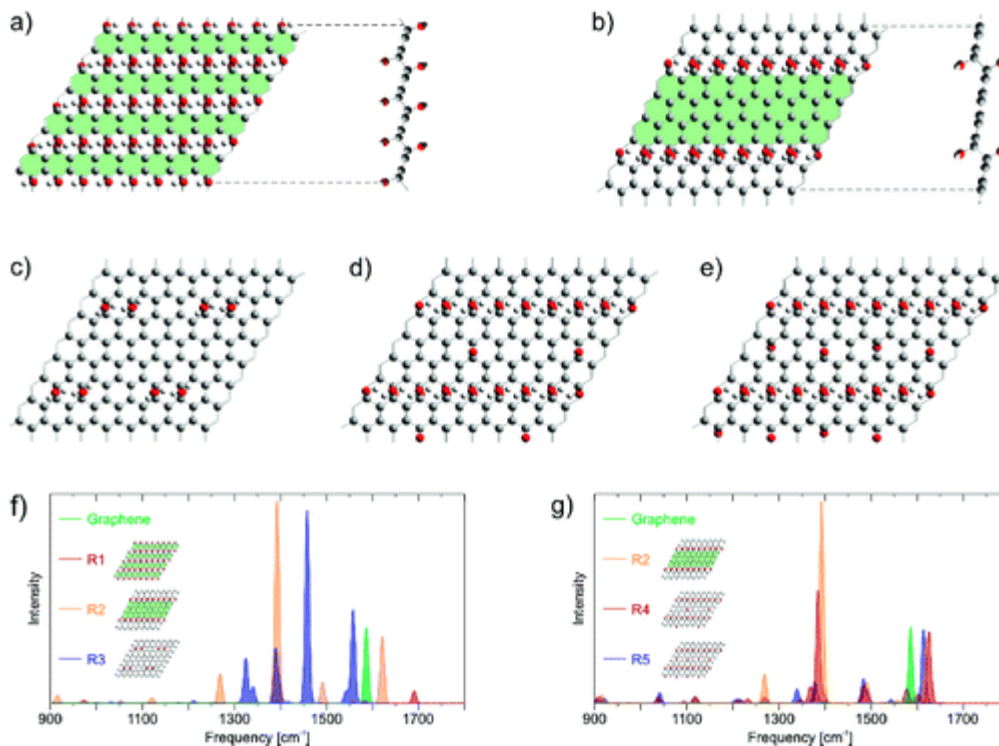


Figure 5 Raman Spectra for Several Possible Graphene Oxide Structures

In Figure 5b, a similar structure known as R2 is portrayed, in which the ribbons are widened yet otherwise indistinguishable from R1. Figure 5c displays a third structure, named R3, where half of the oxygen groups are removed from the R2 model, eliminating the ribbon-like structure of the graphene. Figures 5d and 5e represent intermediate structures between R2 and R1, adding extra pairs of oxygen atoms between the rows of oxygen in R2.

The Raman spectra for each of these structures are shown in Figures 5f and 5g, where Figure 5f specifically compares pristine graphene with structures R1, R2, and R3 while Figure 5g compares graphene with R2, R4, and R5. The study observed how most of the structures featured a G peak that was blue-shifted relative to pristine graphene. It was concluded that this shift was the result of the presence of double bonds between the graphene and oxygen atoms. Because double bonds resonate at higher frequencies than single bonds, they would cause a

shift upward in the frequency of the characteristic G peak. This trend was expectedly most pronounced in the R1 structure, which has the highest density of oxygen atoms. By contrast, the R3 model, which contains the fewest number of oxygen atoms, doesn't display this phenomenon at all and instead has a G peak that is effectively the same as that of graphene. Additionally, almost all of the structures also contain a large peak located around 1390 cm^{-1} , which represents the D peak of graphene. This plot thus shows that graphene oxide displays a similar characteristic G peak as graphene, yet can be distinguished from graphene by the presence of such a large D peak.

This high intensity peak originates from the fact that the oxygen atoms act as defective particles on the graphene surface, which "turn on" the D peak of graphene. However, the spectra for some of the structures did not have a noticeable D peak at all. Specifically, structures R1 and R5 contained the blue-shifted G peak but had no detectable D peak. The study explains that for R1, the presence of such a large number of oxygen atoms leads to correspondingly thin graphene ribbons. Because of this, the R1 structure does not contain any large areas of sp^2 hybridization but instead only has several smaller such regions, causing much smaller intensity G and D peaks in the resulting Raman spectra. The D peak itself is small enough to not even be visible. By contrast, the R2 structure contains much larger graphene ribbons and thus much higher intensity G and D peaks. As R5 is an intermediate between R1 and R2 that is closer to the R1 structure, it is reasonable to expect the hybrid spectrum seen in Figure 5g, where the D peak is relatively small and the G peak is roughly normal for graphene. Clearly, then, this study illuminates the general understanding of Raman spectroscopy of

graphene oxide by providing possible models of graphene oxide structure and corresponding Raman spectra that allow one to identify the characteristic peaks and comprehend their likely origins.

In contrast to Raman spectroscopy, SEM utilizes a highly focused electron beam to characterize materials. The electron beam is produced by an electron gun with a tungsten cathode and passed through a series of lenses that focus the beam directly on the sample. The electrons then interact elastically with the specimen, producing secondary electrons, and both the backscattered electrons from the incident beam and the secondary electrons from the sample are detected by specialized detectors. The experimental apparatus of an SEM machine are given below in Figure 6. The principle advantage of SEM is its high resolution, which can

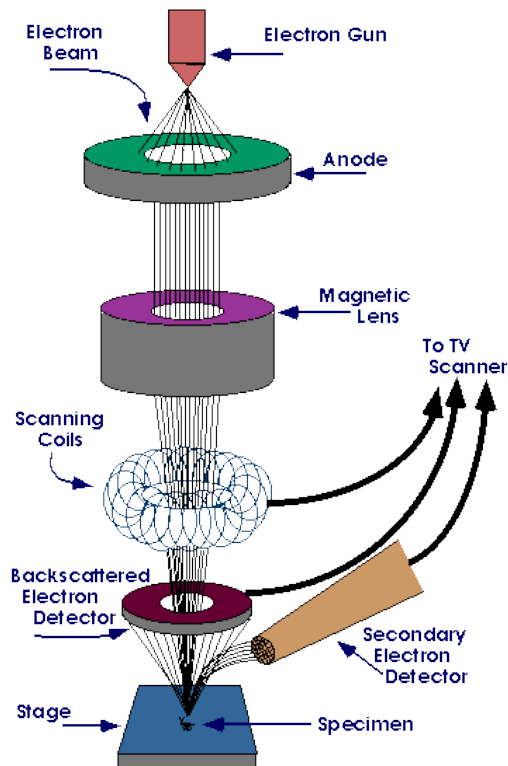


Figure 6 SEM Apparatus¹²

reach the sub-nanometer range. Thus, SEM is able to produce very high quality images of virtually any nanoscale structure, and it works well with a wide range of specimens, similar to Raman spectroscopy. However, also like Raman spectroscopy, SEM is only able to image a small region of the sample such that imaging materials on the macroscale level can take several days. In addition, SEM is highly destructive toward the sample due to the fact that imaging is done through high-energy electrons as opposed to massless photons of light. Another significant disadvantage of SEM is its high cost, which is generally on the order of several hundreds of thousands of dollars.

The literature provides several examples of SEM characterization of graphene-like sheets. Specifically, SEM has been utilized to observe the structure and overall quality of CVD-grown graphene¹³, and the resulting images of the study are shown in Figure 7. Figure 7a portrays SEM of graphene produced after 30 min of CVD growth on copper. From the image, one can clearly observe the various grains in the sample. Also, the striated lines demonstrate how the underlying structure of the copper substrate translates to the graphene. The thin copper sheets used as substrates for CVD growth of graphene are generally produced by rolling techniques, which impart striated stress lines onto the copper. From the SEM image in Figure 7a, it can be concluded that these stress lines are transferred to graphene grown on such a copper surface. This study, therefore, highlights the usefulness of SEM imaging of graphene, as it is able to provide insightful knowledge of how the structure of a substrate material affects the resulting graphene structure in CVD processes.

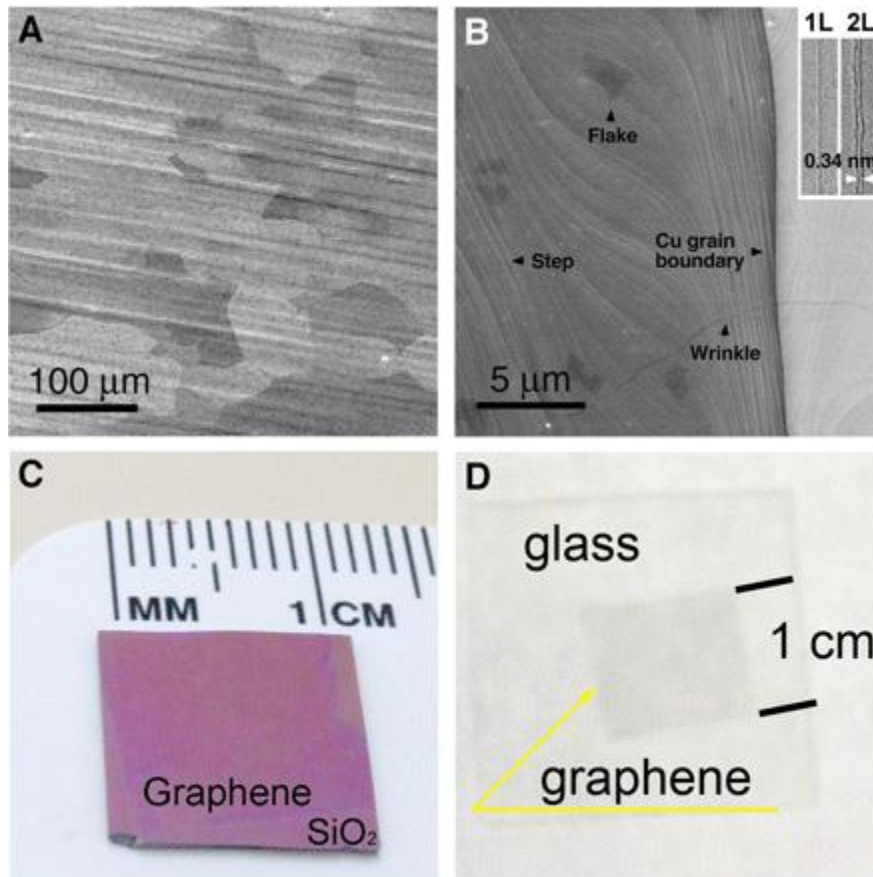


Figure 7 SEM of CVD-Grown Graphene on Copper Substrates

Figure 7b shows a SEM image of the same sample focused on a single grain boundary edge. This image demonstrates the high resolution of SEM images, as it is able to identify several subtle features of the graphene surface. Not only is the grain boundary clearly identifiable, but one can also observe steps within the graphene that reveal the non-uniformity in the surface. Also, multiple layers of graphene can be distinguished in the sample. Specifically, the figure highlights bilayer and trilayer graphene flakes present in the graphene. Wrinkles in

the sample due to graphene folding can also be identified, showing the ability of SEM to characterize even these features of graphene. Figures 7c and 7d show optical images of the CVD graphene as it is transferred to SiO₂ and glass surfaces, respectively.

SEM has also been studied as a method of characterizing graphene oxide. In particular, one study from the literature investigated the hydrophilicity of graphene oxide sheets. The authors concluded that graphene oxide is hydrophilic at the edges and hydrophobic in the interior basal plane. Several experiments were then performed to analyze the effect of various parameters, such as pH and physical size, on the hydrophilicity of graphene oxide. SEM proved to be instrumental in confirming the effect of the size of graphene oxide sheets on their hydrophilicity. Figure 8 shows SEM images of graphene oxide deposited onto Si wafers. In Figure 8c, the flakes were drop-casted directly into the Si wafer from a stock dispersion, and a scheme of the drop-casting method is given in Figure 8a. From this image, the authors of the study observed a roughly uniform mixture of large graphene oxide flakes (> 5 μm) and smaller flakes (< 1 μm). In comparison, Figures 8d and 8e displays SEM of graphene oxide deposited onto a Si wafer through LB assembly. The graphene oxide flakes used in this deposition method came from the same stock solution used in the drop-casting technique. A schematic image of the LB assembly method is given in Figure 8b. Figure 8d specifically depicts an image of the surface of the aqueous solution, revealing the exclusive presence of large sheets of graphene. In contrast, Figure 8e displays an SEM image of a region within the aqueous solution, showing that only very small flakes of graphene are present. From this, it was confirmed that smaller flakes, which have a much higher edge-to-interior ratio, are in fact

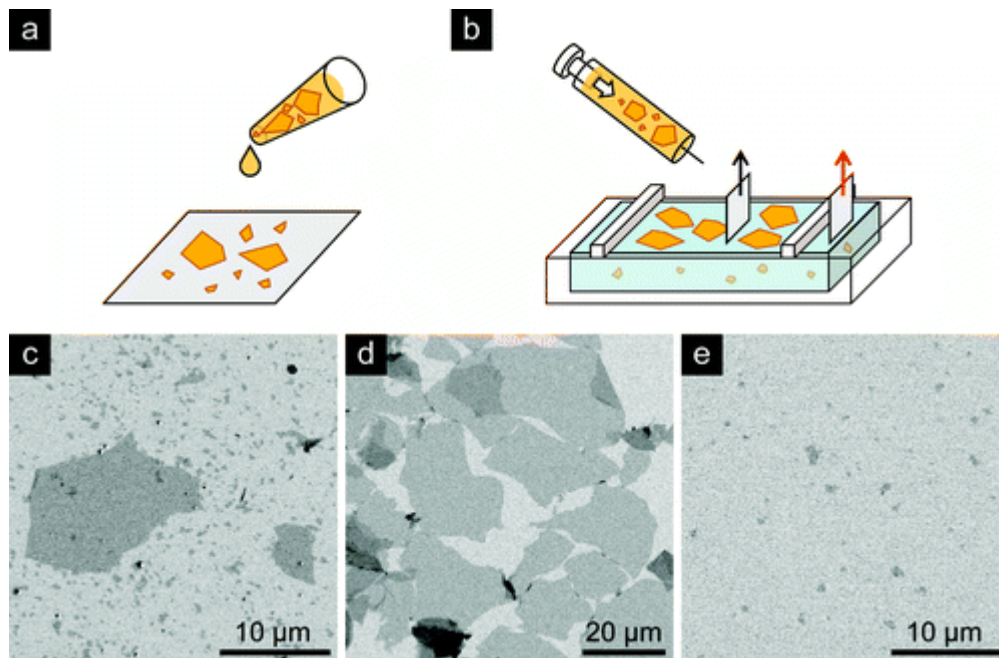


Figure 8 SEM of Graphene Oxide Flakes on Si Wafers

significantly more hydrophilic than larger graphene oxide sheets. Thus, in this study, SEM proved vital in demonstrating the effect of the size of graphene oxide flakes on the hydrophilicity of such sheets.

TEM is a characterization technique that displays many of the similar characteristics of SEM. Like SEM, TEM utilizes an electron beam produced by an electron gun and focused through internal mirrors. The electrons scatter elastically off the sample and the transmitted electrons are then detected by the machine. The details of a typical TEM are given in Figure 9. TEM displays many of the same advantages and disadvantages as SEM. TEM is able to image even higher resolutions than SEM, but is also significantly more expensive, often costing in the range of millions of dollars. This technique is also very destructive and requires long imaging times to characterize a macroscopic sample.

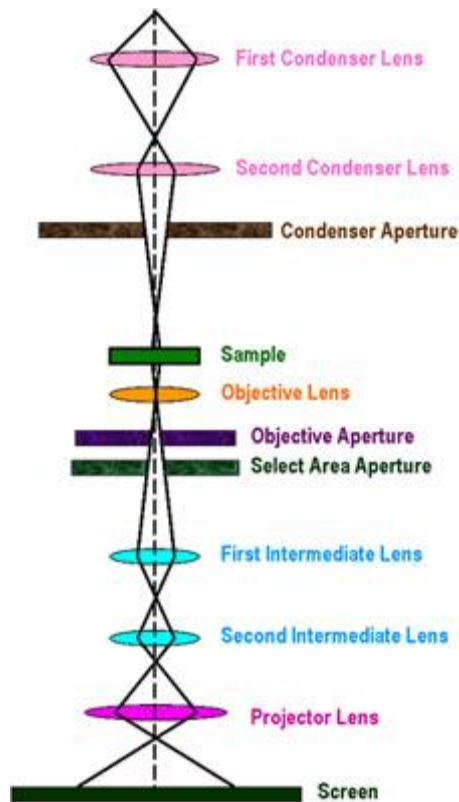


Figure 9 TEM Apparatus¹⁴

Along with Raman spectroscopy and SEM, TEM has also been utilized abundantly as a graphene characterization method in literature. One study in particular analyzed graphene's ability to aid in the imaging of the tobacco mosaic virus (TMV)¹⁵. The TEM images of the graphene/TMV mixture are given in Figure 10. The tobacco viruses can be easily distinguished as the darker, rod-like structures in the images and the contrast value was determined to be on the order of 0.3, showing good overall contrast. The study attributes this high contrast between the viruses and the graphene background to the inherently high transparency of graphene sheets. However, not only does TEM clearly confirm the presence of the tobacco viruses embedded into the graphene structure, it also reveals areas of contamination in the sample. The study identifies two types of contamination from the image. The first form of

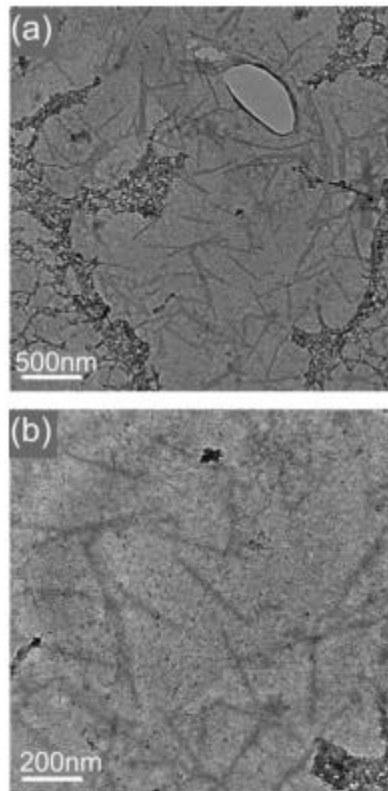


Figure 10 TEM of Tobacco Mosaic Virus (TMV) Supported by Graphene Sheets

contamination is depicted as the patchy, high-contrast regions overlapping the lighter, rod-like virus structures. It was determined by the study that these contaminated regions resulted from improper transfer of the graphene sheets between substrates before imaging, leaving behind residual material from the transfer solutions. The other form of contamination can be seen as the hole in Figure 10a and is the result of the fact that the tobacco virus was used in the form of a suspension. The hole observed in Figure 10a resulted from the presence of molecules in the suspension that were not fully centrifuged out before the viruses were deposited onto the graphene surface. The ability to identify and characterize the expected features of the graphene/TMV mixture as well as the defective aspects of the structure demonstrate the usefulness of TEM as a method of characterizing nanoscale materials such as graphene.

In addition to studies on graphene, TEM has also recently been applied as a method of characterizing graphene oxide. In particular, as graphene oxide has been extensively studied as a precursor material for the fabrication of graphene, it has become increasingly important to have high resolution investigations of the atomic structure of graphene oxide and its correspondingly reduced counterpart. One such study has investigated the effectiveness of producing graphene from graphene oxide through TEM and Atomic Force Microscopy (AFM) characterization¹⁶. Figure 11 displays representative TEM images of the graphene oxide sheets used in their experiments.

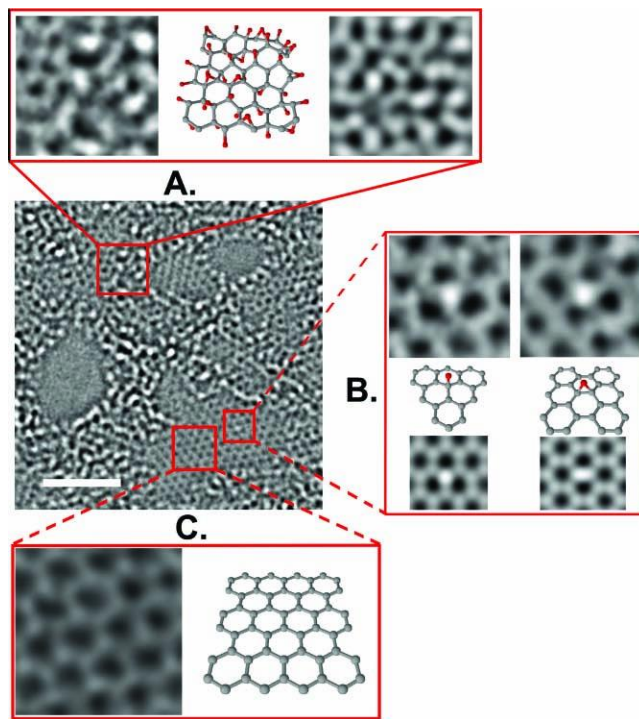


Figure 11 TEM of Graphene Oxide

The central image in the figure shows the results of the TEM analysis of a representative graphene oxide sample. Subset A of Figure 11 focuses on a segment of this image containing oxidized material. A ball-and-stick model for this region is also estimated, where the red atoms

represent the placement of oxygen and the white atoms denote the underlying graphene structure. To the right of this image in subset A is a simulated TEM image based on the ball-and-stick model. Similar analysis occurred for subsets B and C. In subset B, a mobile white spot was examined at two different positions in the pristine graphene region of the sample. Models were then constructed of each of these locations in the structure, and it was assumed that the white spot represented an oxygen atom. Thus, two structures involving this proposed mobile oxygen atom can be seen in subset B. Simulated TEM images of these models were also created and are shown below the models for each structure. Subset C also shows a focused TEM image of the pristine graphene region and a ball-and-stick model of the pure graphene. The study observes how the oxidized and pristine regions can be clearly identified in the image, showing that the oxidation technique used for the sample was imperfect. Also, it was concluded that the simulated TEM images for each region were very similar to the observed image of the region, demonstrating that the models for each region were accurate.

Chapter 3: Applications of Large-Area Graphene and Graphene Oxide

Though the discovery of graphene has already been a significant scientific breakthrough, practical application of this material is hindered by its current small-scale production. Pristine graphene can be readily obtained at the micrometer level, but producing uniform single-layer graphene on the centimeter scale and beyond has generally proven difficult, with chemical vapor deposition (CVD) being the best method to fabricate graphene of this size, though there are still challenges in improving the quality of the graphene^{17,18,19}. One study reports that graphene sheets up to several feet in length have been produced through CVD²⁰. However, large-area graphene does display numerous uses in a wide variety of applications. For instance, graphene has already been shown to be an excellent conductor material for solar cell applications^{21,22}. Larger graphene sheets allow graphene to be used in macroscale solar cell devices that are competitive with those that are currently on the market. Large-area graphene also proves useful as a structural support material. It has been reported that large sheets of graphene and carbon nanotubes can be interwoven to form rope-like structures, which can then be used to reinforce steel beams and cables in a variety of structural applications²³.

Similarly, graphene oxide has increasingly become a widely-applied and valuable material. In particular, graphene oxide displays a clear affinity for cancer cells, allowing it to be an effective material for targeted drug delivery. One study reports functionalized nano-graphene oxide sheets were used as a shell to transport treatment drugs to cancerous cells in mice, significantly reducing the number and intensity of the infected cells²⁴. In addition, transistors require patterned conductive and oxide regions on a substrate and graphene has been demonstrated as an effective contact conductor for transistors. Therefore, patterned graphene

oxide has increasingly become more valuable as a transistor material with minimal heat produced²⁵. The most significant application of graphene oxide in recent studies, however, is as a precursor for the fabrication of graphene. Graphene oxide can be simply reduced to form pristine graphene, yet because the oxygen atoms tend to create wrinkles in graphene oxide, the resulting graphene produced by this method will also contain numerous wrinkles. Due to this effect, reduced graphene oxide generally performs worse than typical flat sheets of graphene. Nevertheless, reduced graphene oxide sheets have proven to be highly effective in a variety of practical applications^{26,27,28,29,30}.

Chapter 4: Background and Motivation for FQM

Since graphene and graphene oxide display great usefulness in a wide range of applications, proper characterization of these materials is highly important. However, as mentioned previously, the common characterization techniques of Raman spectroscopy, SEM, and TEM exhibit severe disadvantages in imaging large-area graphene and graphene oxide sheets. Thus, this study proposes the method of fluorescence quenching microscopy (FQM) as a means of overcoming these disadvantages while still providing good-quality characterization. A schematic of a typical fluorescence microscope is shown in Figure 12. As observed in the figure, a fluorescence microscope operates using white light that passes through a filter, or series of filters, such that only a narrow spectrum of light reaches the surface of the specimen. In fluorescence microscopy, samples are coated with fluorophores, which become excited when they absorb light incident to the sample. The fluorophores then emit light that is usually of a lower frequency than the incident light, and this emitted light is detected by the microscope's

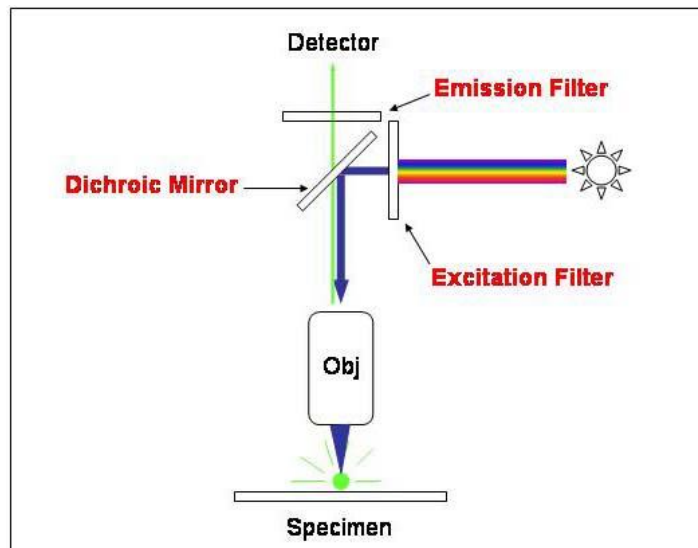


Figure 12 Schematic of a Fluorescence Microscope³¹

built-in detector. Different components of the sample will accumulate different concentrations of fluorophores. Thus, regions with higher fluorophore concentrations will emit higher intensity light than other regions, allowing a contrast between regions on the specimen to be easily seen through the microscope.

Fluorescence microscopy demonstrates several advantages over more conventional characterization techniques. Because this technique uses visible light instead of electrons, fluorescence microscopy is a much less destructive procedure than SEM or TEM, which means that samples imaged by this technique can continue to be used for actual applications after imaging. This provides the distinct advantage that one can characterize the exact sample that is being used for a given application instead of characterizing a representative sample of a batch. Along with this, fluorescence microscopes can image regions hundreds of micrometers in length instantaneously, which means that samples on the order of inches in length only require a few hours to characterize. This then vastly improves the imaging time necessary for other common processes such as Raman spectroscopy, SEM, and TEM. Fluorescence microscopes are also far less expensive, costing only around \$10,000 on average.

The use of fluorescence microscopy has been studied extensively throughout the literature, primarily for the purpose of biological imaging. One study shows how fluorescence microscopy was used to determine the orientation of components of cell membranes³². In the study, fluorescence microscopy provided a useful way of determining several local properties of membranes such as its local viscosity. This method also allows for a study of protein-protein and protein-lipid interactions within the membrane, along with giving an overall picture of the membrane morphology as a whole. Figure 13 shows the results of their experiments. In Figure

Figure 13a, a schematic of a typical fluorescence anisotropy experiment is given while Figure 13c shows a scheme of the microscope setup. The anisotropy of the fluorescence gives information about the orientation and position of proteins along the cell membrane. Figure 13b displays the relationship between this anisotropy and the membrane's viscosity, revealing an asymptotically increasing relationship between these two variables. Both of the fluorescent dyes used, INDO-1 and BCECF, demonstrated this trend. Figure 13d gives the final fluorescence images of the overall intensity, anisotropy, and cluster size of proteins in the cell. The intensity and anisotropy images can be used to derive the size of the protein clusters, giving valuable information regarding the membrane morphology and interactions between the proteins on the membrane.

In addition, fluorescence microscopy has been shown to be a reliable technique for comparing the effectiveness of cancer treatments. In one study, fluorescence microscopy was

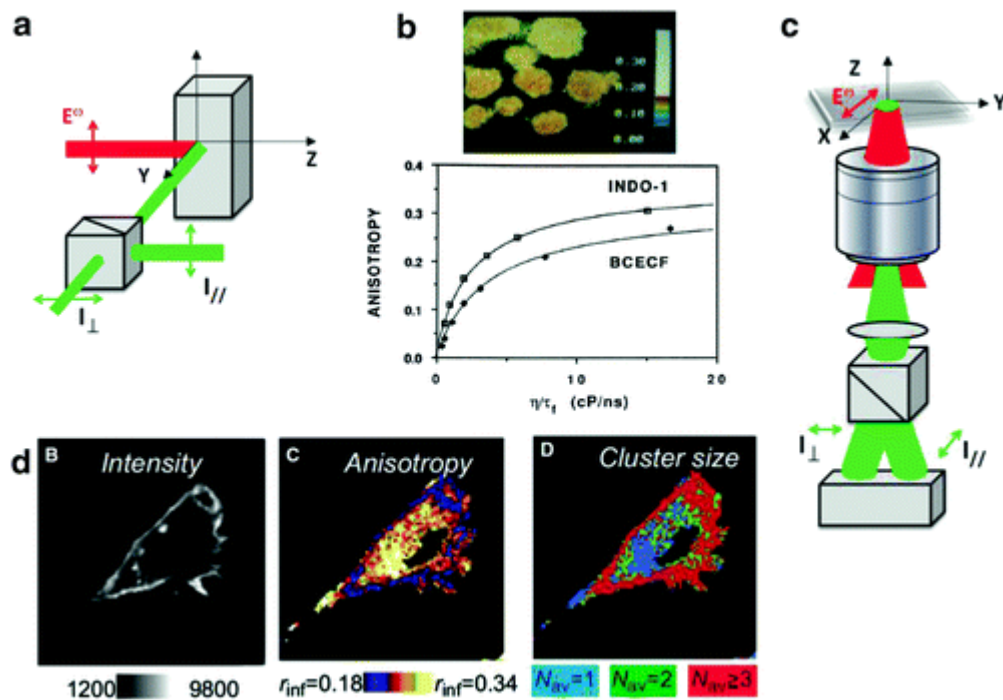


Figure 13 Fluorescence Microscopy of Biological Cells

compared with fluorodeoxyglucose-positron emission tomography (FDG-PET), which is the standard method of determining cancer drug effectiveness³³. These two techniques were used to compare the drug trastuzumab to a control of IgG. The results of the study are shown below in Figure 14. In Figure 14a, fluorescence images were taken using a dye with an affinity for NADH and FAD, which are both redox factors that affect the metabolic activity of cells and are thus commonly used to identify the presence and severity of cancer. Figure 14a, then, shows the corresponding fluorescence of these chemicals in cancerous cells treated with both the control and trastuzumab. The redox ratios of NADH and FAD are also derived from these images. In Figures 14b and 14c, the redox ratios and NADH lifetime as a function of the number of days after treatment are given. It is clear from these plots that a noticeable distinction can be

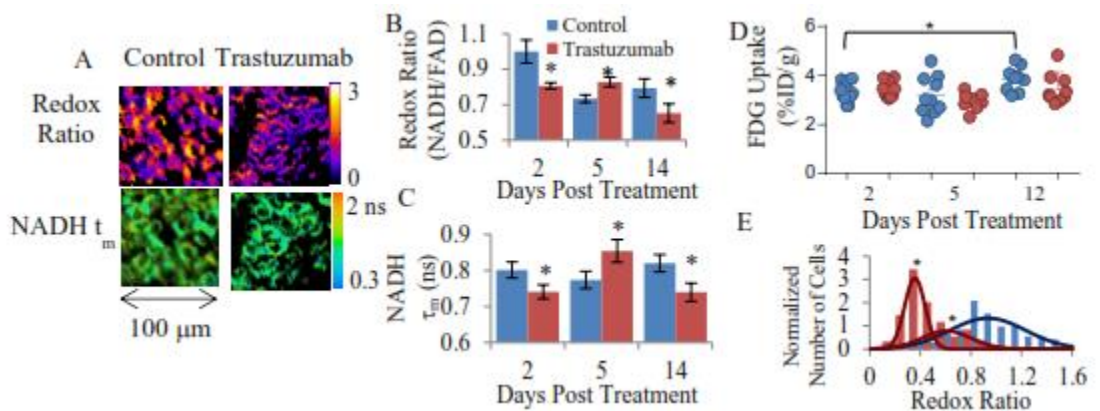


Figure 14 Comparison of Fluorescence Microscopy and FDG-PET in Determining Cancer Drug Effectiveness

made between the control and trastuzumab treatments. Because of this contrast, it is possible to compare the effectiveness of these therapies and identify the one with superior performance. Also, Figure 14e depicts the number of living cells for each treatment as determined by fluorescence microscopy. Again, the two treatments can be easily contrasted, showing that the trastuzumab treatment leaves more cells alive than the control and suggesting

that it is more effective overall. Figure 14d, however, shows the results of the FDG-PET technique in determining the percentage of FDG uptake in the control versus trastuzumab treatments. Unlike the experiments with the fluorescence microscope, the tomography results show no distinction between the two treatments, making it difficult to use this technique as means of evaluating cancer drug therapies. Thus, these results reveal fluorescence microscopy to be a superior method of comparing treatments for cancer than the standard method of FDG-PET.

Another emerging use of fluorescence microscopy studied in literature is in mapping changing concentrations of glucose in pancreatic beta cells³⁴. The fluorescence data showing the distribution of glucose in these cells is given in Figure 15 below. The fluorescence dyes used in this experiment were citrine and enhanced cyan fluorescent protein (ECFP) and the normalized ratio was of the fluorescence intensities emitted by these dyes was used as a measure of the overall fluorescence intensity. Figure 15a gives the fluorescence ratio as a function of time, showing that the fluorescence intensity and thus the glucose concentration remain effectively unchanged over time. Also, Figure 15d reveals how the fluorescence ratio increases as the glucose concentration expectedly increases. Figures 15b and 15c show fluorescence images of individual pancreatic cells at two different glucose concentrations whereas Figures 15e and 15f display images of clusters of cells at the same glucose concentrations. In Figure 15g, the fluorescence ratio for several other glucose concentrations is given while Figure 15h shows the images associated with three specific concentrations from Figure 15g. Figure 15i displays the rate of change of the fluorescence ratio over time as a

function of the concentration of glucose. Through this analysis, not only was the distribution of glucose molecules effectively observed, but it was also concluded that glucose concentration

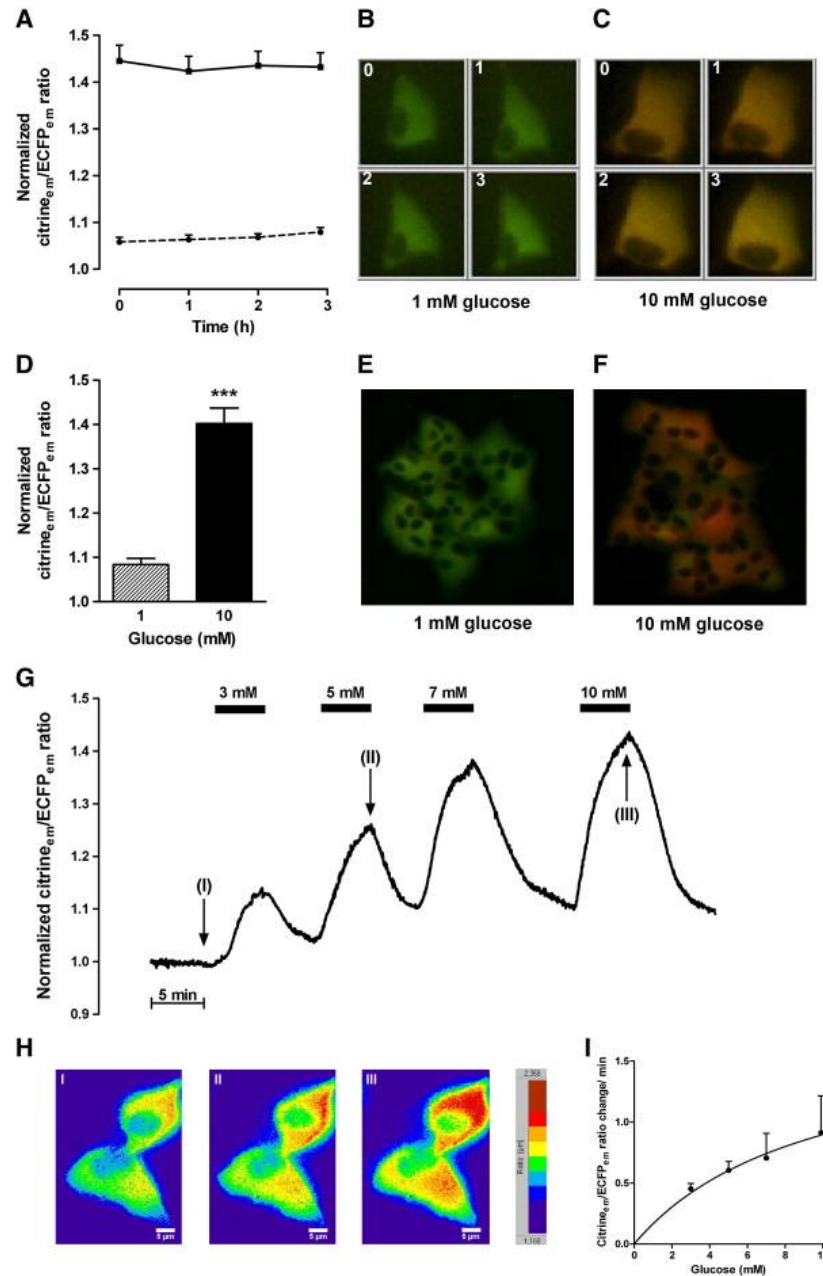


Figure 15 Fluorescence of Glucose in Pancreatic Beta Cells

does not oscillate with time and thus does not play a direct role in the pacemaking activities of the cell. Also, the authors further studied the Ca ion concentration in the cell and it was shown through similar studies of the fluorescence ratios that when glucose levels reach a certain threshold, the Ca ion concentration begins to oscillate, demonstrating that glucose does play an indirect role in the pacemaking activities of pancreatic cells. Clearly, the use of fluorescence microscopy allows this type of study to be feasible.

The effect of fluorescence imaging techniques on biological tissues has also been widely investigated. One such study examined the tolerable light doses for U373-MG glioblastoma cells functionalized with fluorescent molecules compared to native cells without fluorescent capability³⁵. The data acquired from this study are summarized in Figure 16 below. In the figure, the plating efficiency refers to the percentage of cells in a culture that survive radiation at a given dosage of light. Native cell cultures were compared using light with 375nm, 514nm, and 633nm wavelengths. As expected, the cultures illuminated by the highest wavelength light source survived at the highest dosages. Cells incubated with laurdan fluorescent markers are also described in the figure, and show a steep decrease in plating efficiency as a function of dosage, much faster than for any of the healthy, native cells. The data thus demonstrates how fluorescent markers seem to have a detrimental effect on biological tissues, and the study concluded that fluorescent markers may generally be toxic to cells, especially as the plating efficiency decreases non-linearly with light dosage. This study, then, sheds light on the effects of fluorescence microscopy on biological samples and makes an attempt to quantify these effects.

Fluorescence microscopy has been further applied to the study of oxidative stress in cellular activity. Specifically, it was determined that fluorescence microscopy was able to selectively target the products of oxidative stress in Chinese hamster ovary cells³⁶.

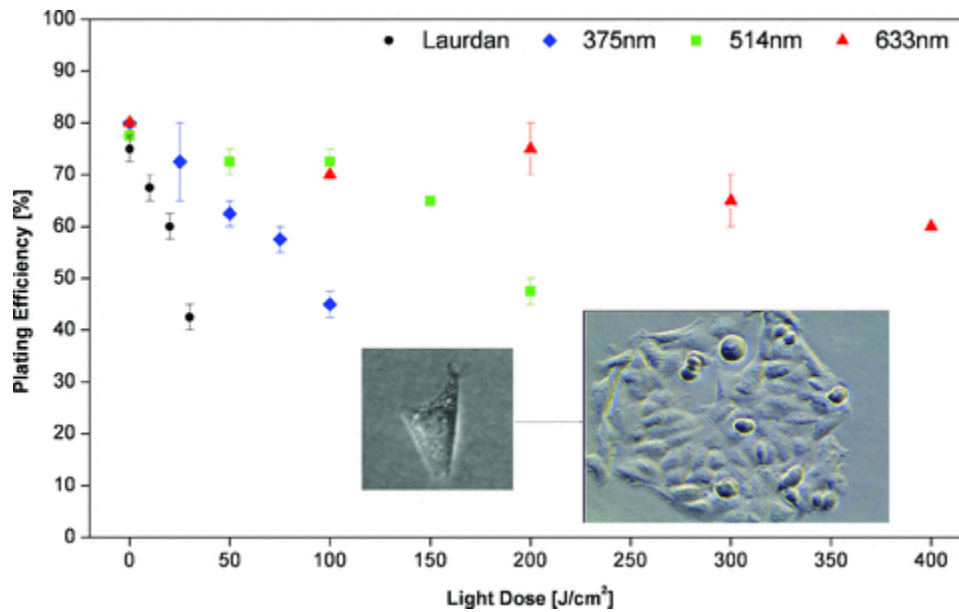


Figure 16 Viability of Cells with Fluorescent Markers

Oxidative stress refers to a state of imbalance between the concentrations of prooxidants and antioxidants in cells. This imbalance leads to the overproduction of peroxides and free radicals that have been linked to an increased risk of Parkinson’s disease³⁷, cardiovascular aging³⁸, and Alzheimer’s disease³⁹. The study utilized the common fluorophores of anthracene and fluorescein functionalized with nitroxide radicals. Due to the presence of the radical species, the fluorescence of the fluorophores becomes almost entirely quenched. However, the nitroxides react in the presence of oxidative radical species, thus de-functionalizing them from the fluorophores and eliminating the quenching effects. Because of this, these particular fluorescence markers are able to produce a distinct contrast between regions where oxidative

stress occurs and doesn't occur in cells. The results of the study are as shown in the fluorescence images in Figures 17 and 18.

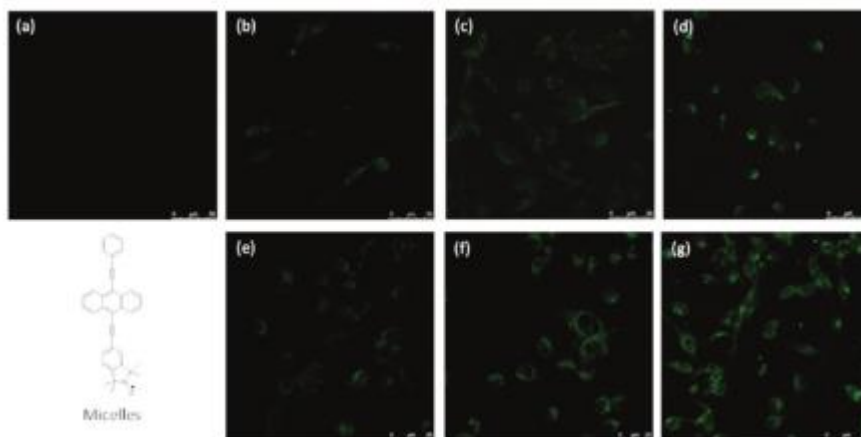


Figure 17 Fluorescence Microscopy of Oxidative Stress Products

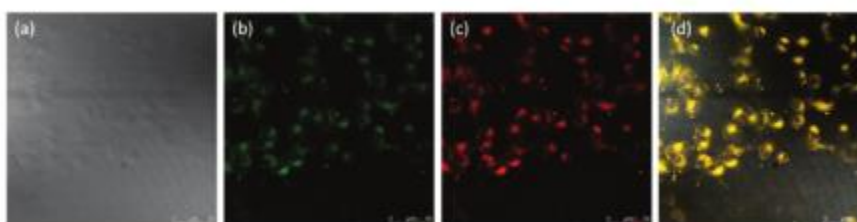


Figure 18 Comparison of Fluorescence Microscopy with CellROX Deep Red

Figures 17 and 18 show the fluorescence response of the nitroxide fluorophores to varying concentrations of H_2O_2 , which is a common byproduct of oxidative stress. Figure 17a represents a control image containing no fluorophores or peroxide material. Figures 17b – d display images of solutions of $5 \mu M$ nitroxide fluorophores with $0 \mu M$, $100 \mu M$, and $200 \mu M$ H_2O_2 , respectively. Clearly, as the concentration of hydrogen peroxide increases from Figure 17b to 17d, the degree of fluorescence correspondingly increases, confirming that radical species react with the nitroxide groups, eliminating the quenching effects on the fluorophores.

Similarly, Figures 17e – g show images of 10 μM nitroxide fluorophores with 0 μM , 100 μM , and 200 μM H_2O_2 . As in Figures 17a – d, Figures 17e – g display increasing fluorescence as the peroxide concentration increases. Also, as expected, the amount of fluorescence increases as the concentration of fluorophores increases. The particular nitroxide utilized in these images had a micelle-like structure, which is shown in the bottom-left corner of the figure.

Figure 18 compares the effectiveness of the nitroxide fluorophores in imaging oxidative stress products with the standard characterization technique, CellROX Deep Red. In Figure, 18a, a differential interference contrast (DIC) image is constructed, showing very low contrast overall. Figure 18b displays the fluorescence image using 20 μM nitroxide fluorophores while Figure 18c shows the results using CellROX Deep Red. Figure 18d gives the result of overlaying Figures 18a – c into one comprehensive image. From these results, it's clear that the nitroxide fluorescence produces almost exactly the same image as the CellROX technique, demonstrating that functionalized fluorophores are effective in detecting the presence of oxidative stress and in aiding physicians in diagnosing several serious illnesses.

Along with biological applications, fluorescence microscopy has also been applied to the study of graphene. Fluorescence quenching microscopy was used to characterize centimeter-scale graphene sheets and was able to effectively identify regions of defects, the number of layers of graphene present in a sample, and the uniformity of the sheet as a whole⁴⁰. Figure 19 shows the results of this characterization technique. Figure 19a shows the fluorescence image of a region of the cm-scale graphene sheet focused around a defect while Figure 19b depicts an image-processed version of Figure 19a, where the distinctive features of the image are highlighted in various colors. The white regions indicate the presence of the substrate, blue

regions show single-layer graphene, and green regions represent bilayer graphene. Figure 19c shows a corresponding Raman spectrum of the fluorescence image at three specific points indicated by the red, blue, and green dots in Figures 19a and 19b. The Raman data corroborates the identification of the number of layers seen in the fluorescence image. Figure 19d shows the intensity histogram of the fluorescence for the substrate, single-layer graphene, bilayer graphene, 3 or more layers of graphene, and regions where contamination is present. Lastly,

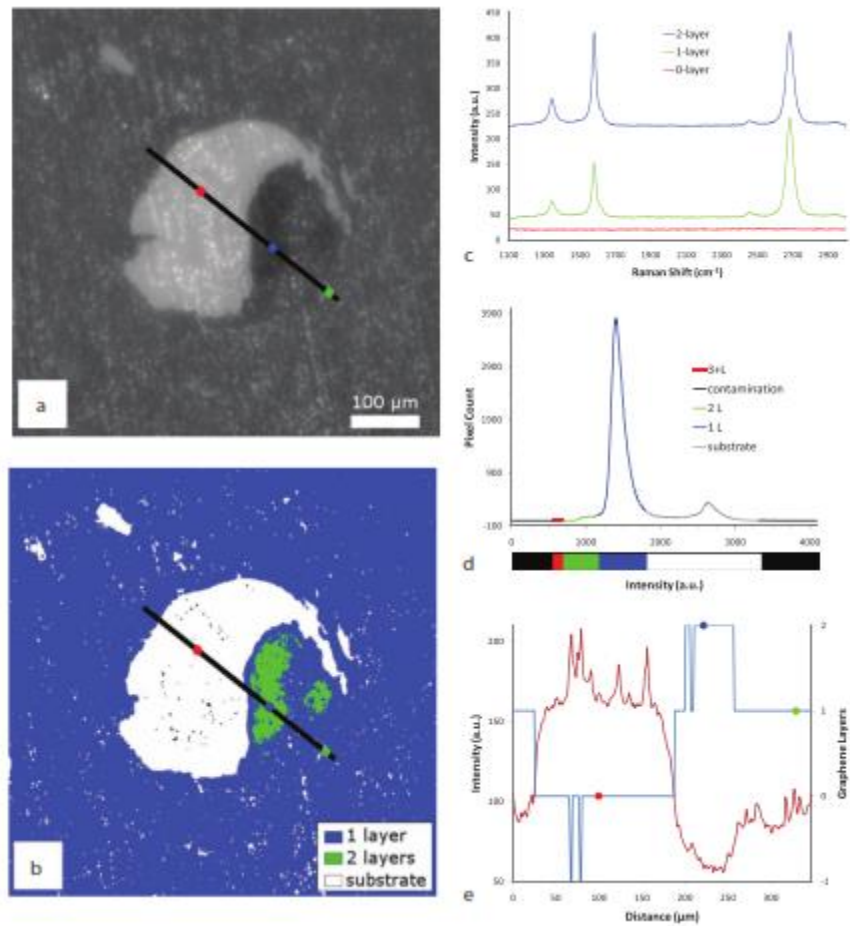


Figure 19 FQM of Centimeter-Scale Graphene

Figure 19e shows the FQM signal along the black line in Figures 19a and 19b. Overall, the FQM technique was shown to give accurate characterization of the location and number of defects in a centimeter-sized graphene sample, the number layers, and the general uniformity.

In addition, FQM has also been studied as a means of effectively characterizing doped graphene sheets. One study utilized FQM to examine whether sufficient contrast can be observed between doped and pristine regions of graphene⁴¹. The results of this endeavor can be viewed in Figure 20. Figures 20a and 20b show the fluorescence images before and after image correction techniques were applied. Figure 20c displays the image-processed results using the computer software, while Figure 20d shows the fluorescence histogram for various components of the sample, with the overall envelope outlined in black. From the images below,

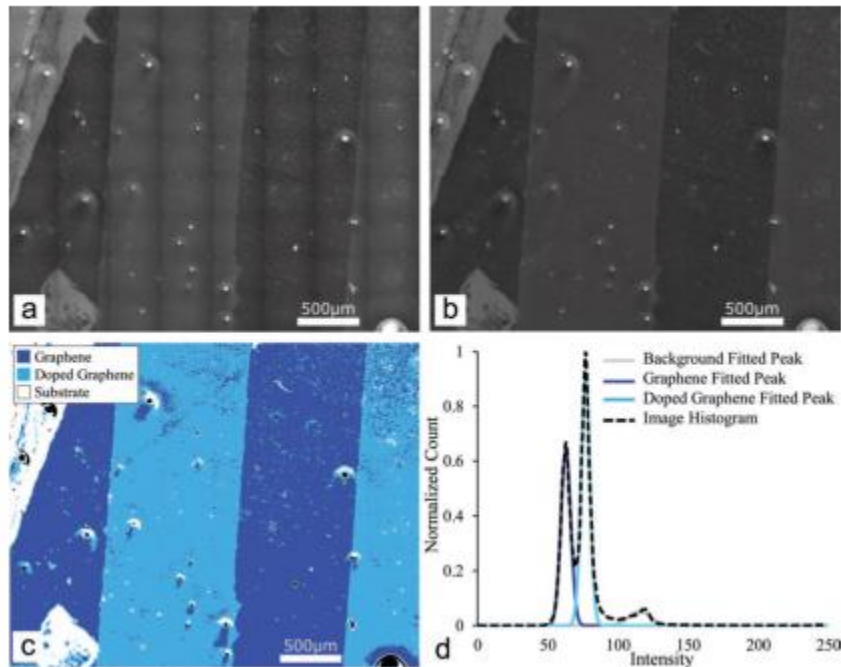


Figure 20 FQM of Doped Graphene

a clear contrast can be identified between the doped and pristine regions of graphene. Thus, fluorescence microscopy was shown to be an effective technique for characterizing doped graphene.

Chapter 5: Theory of FRET

Certainly, fluorescence microscopy has been demonstrated in literature to be a widely applied characterization technique. The central feature of the fluorescence quenching microscopy method proposed in this study is known as Forster Resonant Energy Transfer (FRET). Normal fluorescence microscopy involves shining light of a given wavelength incident to a sample, causing the electrons from a fluorophore in the Highest Occupied Molecular Orbital (HOMO) states to become excited to the Lowest Unoccupied Molecular Orbital (LUMO) states. Some of the electrons' energy is then absorbed by the fluorophore and the rest is emitted as fluorescent light. However, FRET in graphene arises due to the particular atomic structure of graphene. Because graphene has a sp^2 -hybridized structure, there are delocalized electrons present in pi-orbitals orthogonal to the graphene surface. When the graphene is coated with a fluorescent dye and imaged with a fluorescence microscope, the excited electrons in the dye lose some of their energy to the delocalized pi-electrons in graphene, causing the resulting emission of fluorophores on the graphene to be less than that of the fluorophores on the surrounding substrate. This, in turn, allows one to observe a contrast between graphene and the substrate, thus making FQM a viable characterization method.

There are two likely explanations for fluorescence quenching in graphene oxide. Since FRET is the source of contrast between pristine graphene and glass substrates, then it is likely that FRET also plays a role in generating contrast between graphene and graphene oxide. When graphene is oxidized, the internal structure changes from sp^2 to sp^3 hybridization. Because of this, there are fewer pi orbitals and delocalized electrons in graphene oxide, which would lead to less fluorescence quenching due to FRET in graphene oxide than in graphene, allowing a clear

contrast to be observed. FRET has been shown to be a mechanism of quenching in graphene oxide in literature. Particularly, fluorescence quenching due to FRET has been demonstrated between graphene oxide and quantum dots as part of a study using graphene oxide as a sensor for a wide range of biomolecules⁴². FRET has also been shown to allow graphene oxide to be used as suitable material for highly sensitive cancer detection devices⁴³.

A significant alternate theory for the mechanism of fluorescence quenching in graphene oxide relative to graphene has also been developed in literature⁴⁴. It has been proposed that in addition to energy transfer between excited electrons in the dye and the delocalized electrons in the pi-orbitals of the graphene, the electrons themselves also have the ability to transfer from the dye molecules to the graphene, thus quenching the fluorescence of the graphene. Because graphene oxide is much less conductive than graphene, with graphene and graphene oxide work functions of -4.42 eV and -3.50 eV respectively⁴⁵, then it becomes more difficult for electrons to transfer to graphene oxide relative to graphene, creating a disparity in the fluorescence quenching and allowing for a contrast to be observed between these two materials.

Chapter 6: Experimental Procedure

The preparation of the graphene and graphene oxide samples was carried out through CVD growth. Highly pure 25- μm -thick copper sheets were polished to ensure a flat reaction substrate and then treated with acetic acid and deionized (DI) water. The copper sheets were then placed in a quartz tube furnace, a schematic of which is given in Figure 21. As shown in

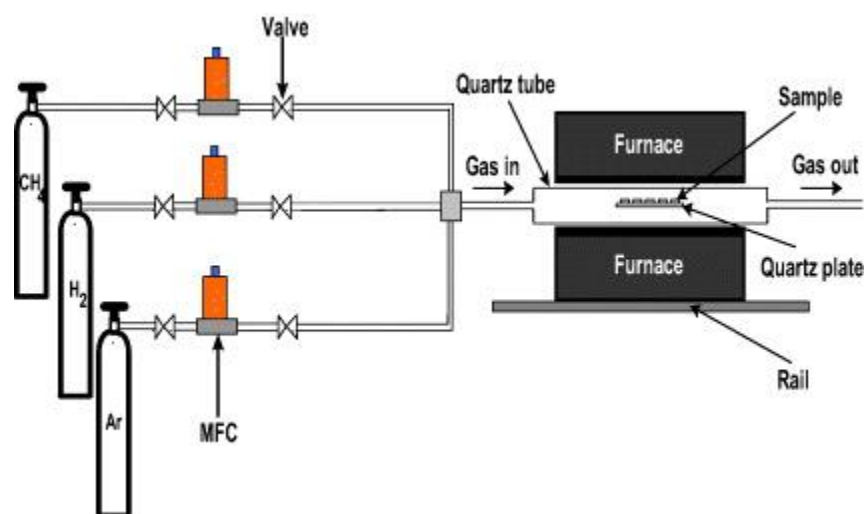


Figure 21 Schematic of a Typical CVD Tube Furnace for Graphene Growth⁴⁶

the figure, the furnace and tube are attached to Ar, H₂, and CH₄ containers, with mass flow controllers (MFCs) that control the rate of gas flow into the furnace chamber. The copper sheets are initially placed in an Ar/H₂ environment at a pressure of 2 torr (200:200 sccm), and the chamber is heated to 1000°C and allowed to remain at that temperature for 30 min in order to thermally anneal the copper. Methane (CH₄) gas is then flowed into the chamber at 20 torr for 20 min (100 sccm) while the temperature is reduced to 25°C at a rate of 20°C min⁻¹. This environment causes the methane gas to deposit carbon atoms on top of the copper sheet, creating a monolayer of carbon with the structure of graphene. For large-area graphene

growth, 2 in x 2 in sheets of copper were used to produce inch-scale graphene sheets whereas for graphene oxide growth, large-area sheets were not a primary concern and thus only centimeter graphene sheets were produced for this purpose.

After growth of the graphene in the furnace, PMMA was drop-coated onto the graphene surface and heated for 10 min at 120°C to dry the PMMA. The graphene sheets were then placed in a FeCl₃ solution to etch away the copper substrate before being cleaned in subsequent solutions of HCl and DI water. Once the graphene samples were cleaned, they were mechanically transferred to glass slides. The slides themselves were prepared by cutting standard microscope slides into 1 in² pieces and rinsing each of them in water and detergent. The slides then underwent further cleaning through sonication in successive solutions of DI water, toluene, acetone, and isopropyl alcohol (IPA) for 30 min each. The slides were then dried in a N₂ gas stream and stored in a vacuum desiccator. Once the graphene sheets were successfully transferred to glass slides, they were dried overnight in order to remove all remaining water particles. In order to remove the PMMA layer, a drop of acetone was placed on each sample before submerging the sample in an acetone solution.

Patterned graphene oxide was achieved by covering half of a graphene sample with PMMA and then allowing it to dry overnight. Oxidation was then performed through an oxygen plasma asher for an interval of only 20s to ensure that the asher oxidizes the graphene rather than etch it away. The PMMA layer was then removed through the method described above. Due to the presence of the PMMA layer, only half of the graphene sample becomes oxidized in the asher. When the PMMA is removed, it leaves behind a region of pristine graphene, thus achieving a graphene/graphene oxide interface.

Once the samples were ready for imaging, they were coated with a fluorescent dye consisting of 0.01 wt% 4-(dicyanomethylene)-2-methyl-6-(4-dimethylaminostyryl)-4 H -pyran (DCM, Sigma – Aldrich) added to PMMA (10 mL, 1.0 wt%, $M_w \approx 120\,000$) and dissolved in toluene (> 99.5%, Fisher Chemical). The dye was continuously stirred by dropping a stirring rod into the solution and placing it on a magnetic stirring plate. Before imaging the graphene samples, the dye was heated at 95°C overnight in order to allow for a uniform dispersion of the DCM dye molecules in the PMMA. The dye was then passed through a 0.22 μm mass filter as it was dropped onto the sample to further disperse the dye. Dispersion of the dye molecules is a significant issue since agglomeration of the dye within the solution itself can lead to unwanted bright spots on the fluorescence image that are not caused by any features of the graphene surface, thus leading to inaccurate characterization of the sample. The graphene then immediately underwent spinning at 3000 rpm for 60 sec with a 2 sec ramp. Once this was complete, coated graphene samples were placed in a vacuum desiccator for 1.5 h to ensure complete evaporation of the toluene solvent, leaving only the dye molecules behind.

Figure 22 gives a schematic of the procedure used to produce the fluorescence images of the graphene and graphene oxide samples. The imaging of the samples was carried out by a BD Pathway 855HT confocal fluorescence microscope with an arc lamp as the light source. Incident light from the microscope was filtered through a 470 nm bandpass filter and a 520 nm dichroic filter before passing through an Olympus 20x objective (0.75 NA) and making contact with the sample. Emitted light was passed through a 542 nm bandpass filter and detected using a CCD camera. The overall resolution of the microscope was determined to be 380 nm. Montage imaging was utilized to capture the entire 1 cm² or 1 in² area of the graphene surface.

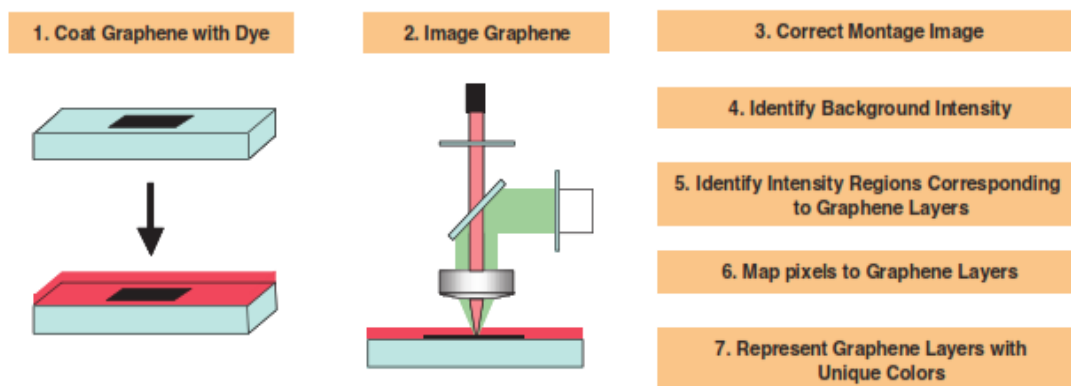


Figure 22 Schematic of the Fluorescence Imaging Technique

In this technique, the microscope scans the surface of the sample while taking a series of smaller, high-resolution images. These images are pieced together as tiles to form a larger montage image. In this study, a 1 cm² montage was constructed in 20-30 min whereas a 1 in² montage was constructed in 2 hrs. The size of each of the tile images was 417 x 318 μm², and BD Attovision software provided control for the microscope and produced the resulting montage images. In order to prevent the software from being overwhelmed by large amounts of information, 4 pixels were collapsed into one pixel for 1 in x 1 in graphene oxide samples while 8 pixels were combined into one pixel for 2 in x 2 in large-area graphene samples.

As shown in Figure 22, the montage image produced from this software was then corrected using homemade Matlab code and ImageJ software, developed by the National Institute of Health, to flatten out the boundaries between the tiles and create a homogenous image. This was accomplished using a flat-field correction technique where a fluorescence image of a plain glass slide was used as a reference for the correction. The correction of the boundary regions between the tiles was accomplished using the following relation:

$$I_{flat}(x, y) = \frac{I_{original}(x, y)}{I_{correction}(x, y)} \times I_{correction}$$

$I_{original}(x, y)$ refers to the intensity recorded from the original fluorescence image, $I_{correction}(x, y)$ represents the corrected intensity recorded from the reference glass slide, and $I_{flat}(x, y)$ is the intensity that is mapped to the resulting flattened fluorescence image.

Furthermore, the intensity of the background substrate was determined and the contrast histogram of the sample was obtained. Intensities were calculated according to the equation below:

$$I_f = (1 - f_Q) \times I_{f0}$$

I_{f0} denotes the intensity of the fluorescent dye by itself, f_Q is the quenching factor, and I_f represents the final fluorescence intensity value at a given point on the sample. Since there is no quenching on the background substrate, one can set $f_Q = 0$ and thus $I_f = I_{f0}$. To find the contrast between the graphene and the background, then, the following equation can be utilized:

$$C = \frac{I_{background} - I_{graphene}}{I_{background}}$$

Substituting I_{f0} for $I_{background}$ and I_f for $I_{graphene}$ yields the following relation:

$$C = f_Q$$

Thus, the contrast between regions on graphene and graphene oxide sheets is entirely determined by the relative quenching of these different regions. The value for $I_{background}$ can

be found by generating a contrast histogram and finding the value of the maximum peak. Once this has been determined, the specific contrast values for each point on the graphene or graphene oxide surface can be computed. By assigning unique colors to each intensity region on the histogram, the various features of the sample can be highlighted for further analysis. The details of the imaging software code are given in the appendix to this study. Once imaging was completed on a given sample, the dye was simply removed by washing the sample in acetone, preserving the actual graphene or graphene oxide to be used in further processing.

Chapter 7: Observations and Results

Figure 23 shows the fluorescence images of a representative 2 in x 2 in graphene sample. Figure 23a shows the original montage image whereas Figure 23b display the results of flat-field correction and final image processing using ImageJ. As can be seen in these images, the various structural details of the graphene are highly defined and easily identifiable. In Figure 23c, a clear distinction can be made between light blue regions that represent the bare substrate, dark blue regions denoting the presence of single-layer graphene, red spots indicating regions of contamination, and bright white spots displaying regions where the dye molecules become

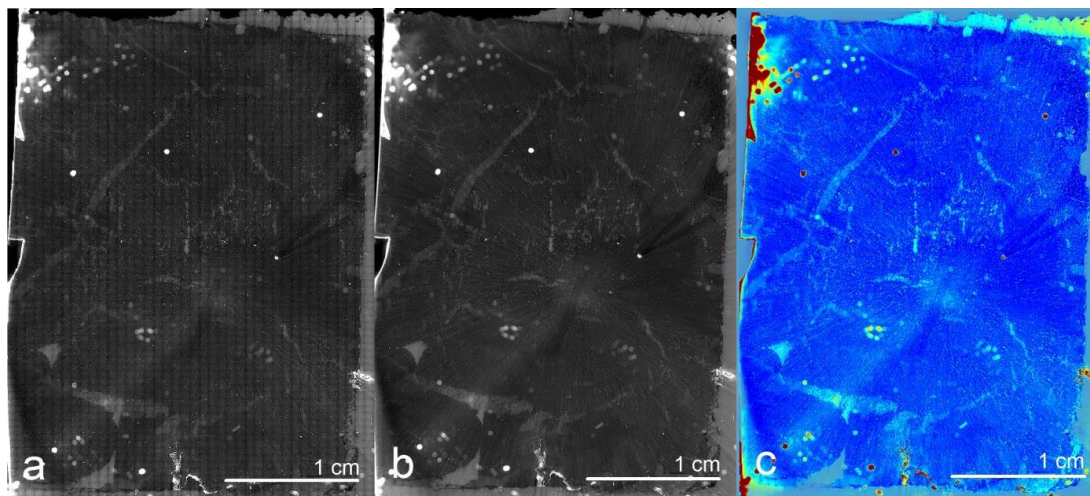


Figure 23 Fluorescence Image of 2 x 2 in Graphene, a) Before Flattening, b) After Flattening, c) With Final Image Processing

agglomerated. Imaging of this sample occurred in less than 2 hrs, which is a substantial improvement over common techniques such as SEM, TEM, and Raman spectroscopy. Because of this advantage in processing time, FQM demonstrates its ability to become a much more scalable characterization process than these other methods, thus making it a preferable technique for practical, macroscale applications.

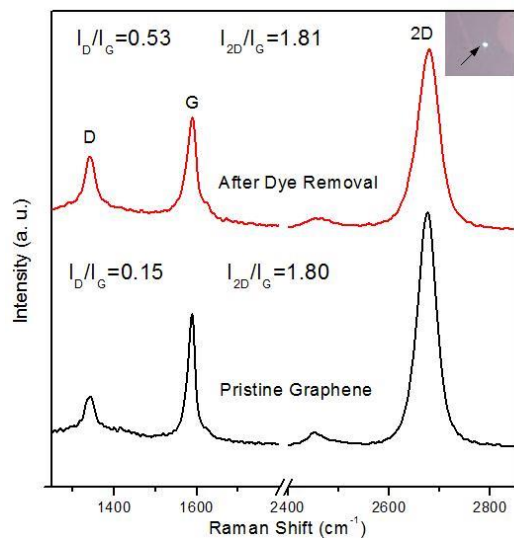


Figure 24 Raman Spectra of Large-Area Graphene Before and After Fluorescence Imaging.

Figure 24 above shows the results of Raman spectroscopy with the black and red curves representing data from before and after fluorescence imaging, respectively. The location on the sample where the Raman data was taken is shown in an inset in the upper right corner of the figure. Each of the two curves shows results consistent with single-layer graphene, with a G peak at 1600 cm^{-1} and a 2D or G' peak at around 2650 cm^{-1} . As shown in the figure, the intensity ratio of the 2D and G peaks remains essentially the same between the two curves, indicating that the graphene was unaffected by the imaging process. Also, the Raman spectrum of the sample before imaging displays a small D peak, representing the concentration of defects in the sample. After imaging, the D peak does increase slightly, which is likely due to an accumulation of defects as the graphene sample is exposed to the environment during imaging rather than any aspect of the imaging process itself. In light of these results, FQM demonstrates itself to be an overall highly nondestructive procedure for characterizing large-area graphene sheets.

Therefore, FQM displays a clear advantage as an imaging method over the more commonly used techniques such as SEM and TEM, which often cause significant damage to the sample, preventing such a sample from being further processed or used in actual applications.

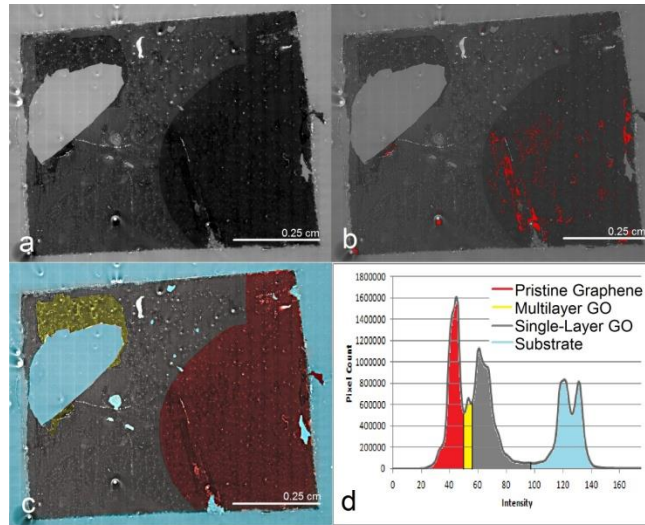


Figure 25 Fluorescent Image of Patterned Graphene Oxide a) Flattened b) Highlighting Regions of Multilayer Pristine Graphene c) With Final Image Processing d) Contrast Histogram of Processed Image

Analysis of patterned graphene oxide by FQM is shown above in Figure 25. As can be seen in Figure 25a, there appears to be four distinct regions of contrast observed in the sample. Figure 25c shows the fully image-processed sample, where the pristine graphene can be identified as the region highlighted in red, which represents the area of the sample that was covered with the PMMA drop and thus shielded from the oxidizing process. The graphene oxide region, then, is shown in gray. The area highlighted in yellow represents a segment of the graphene oxide region that folded over on itself during transfer, creating both a hole in the oxide region and a corresponding multilayer graphene oxide region. The fourth clearly visible region on the sample is the area colored in blue, which denotes the background substrate. The contrast histogram is shown in Figure 25d, with each of the contrast regions being identified in

the histogram with the same colors as used in Figure 25c. The histogram reveals a clear contrast between the pristine graphene and graphene oxide regions, demonstrating that FQM is effective at characterizing patterned graphene oxide samples. It can also be concluded that FQM displays distinct contrast between single-layer and multilayer graphene oxide as well as between pristine graphene and multilayer graphene oxide, demonstrating the sensitivity of FQM in detecting several different material structures on a single sample. The data also show that graphene oxide displays less fluorescence quenching than pristine graphene, confirming the expected results of the theories of FRET and electron transfer mentioned above.

The mean contrast values of pristine graphene, single-layer graphene oxide, and multilayer graphene oxide relative to the substrate are given below in Table 1. As implied in the table, the

Table 1. Mean Contrast Values for Pristine Graphene and GO.

	Pristine Graphene	Single-Layer Graphene Oxide	Multilayer Graphene Oxide
Mean Contrast Value C = $\frac{I_{background} - I_{mean}}{I_{background}}$	0.683	0.526	0.573

higher values of C represent areas of greatest fluorescence quenching whereas lower values imply areas of reduced quenching. The largest contrast difference is observed between the pristine graphene and graphene oxide regions, whereas the difference between single- and multilayer graphene oxide is much less. Certainly, it is expected that multilayer graphene oxide would have a larger contrast value than the single-layer region, since adding an additional layer of graphene oxide doubles the number of pi-orbitals interacting with the incident fluorescent light source. However, the data from this table show that the change in structure from sp² to

sp^3 hybridization as graphene is oxidized has an immense impact on the fluorescence of the material, since even the addition of multiple layers of graphene oxide does not produce as high a contrast value as pristine graphene.

Along with this, the variable contrast function in ImageJ was utilized to highlight darker regions within the pristine graphene region, allowing one to determine the presence of multilayer pristine graphene. The results of this procedure are shown in Figure 25b, with the areas colored red denoting regions of multilayer graphene. Thus, though the contrast difference between the single-layer pristine graphene and multilayer pristine graphene is much less than the difference between any of the other regions in the sample, by using this technique available in the software, additional characterization can be achieved, improving the functionality of FQM as a metrology technique.

The results of identifying different contrast regions on the patterned graphene oxide sample through fluorescence microscopy were corroborated by Raman analysis shown in Figure 26. In Figure 26d, Raman spectra at points in the graphene and graphene oxide regions are shown. As representative points in each of these regions, the spectra clearly support the results of the fluorescence experiments. Both spectra display a graphene-like appearance, with G peaks at 1600 cm^{-1} , 2D peaks around 2600 cm^{-1} , and defective D peaks. As expected, the spectrum in the pristine graphene region contains only a small D peak, whereas the D peak in the graphene oxide spectrum is very large due to the presence of the oxide layer that disrupts the structure of the graphene. From this plot alone, then, the Raman data clearly supports the identification of the graphene and graphene oxide regions from the fluorescence image.

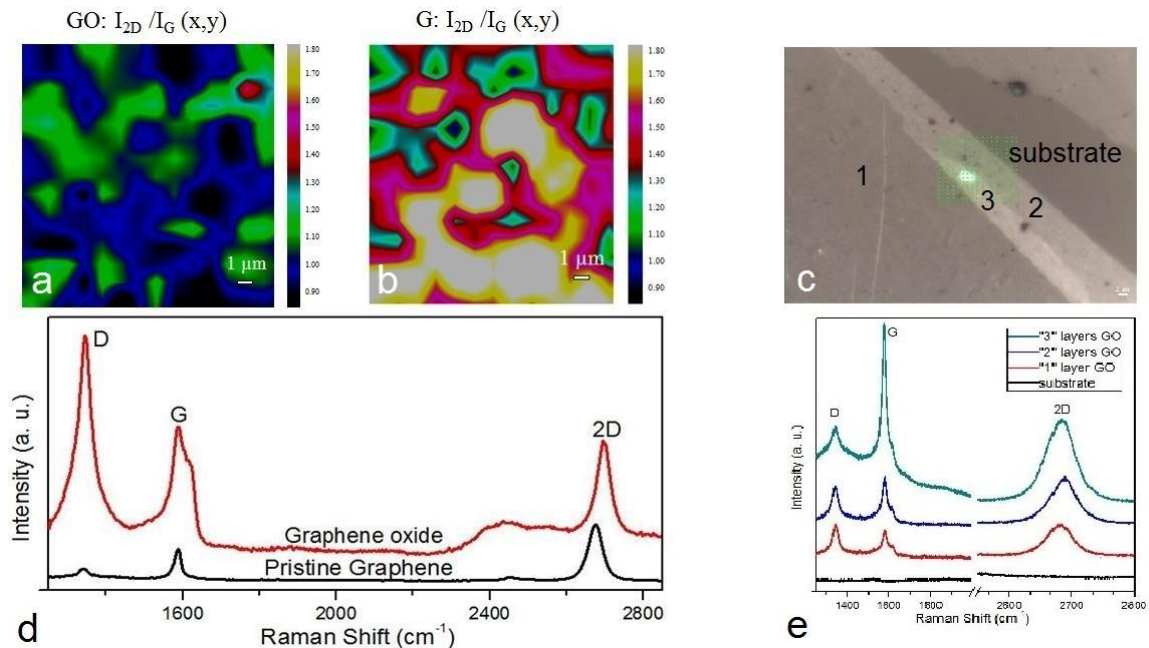


Figure 26 Raman Analysis of Patterned Graphene Oxide a) 2D/G Raman Mapping of the GO Region b) 2D/G Raman Mapping of the Pristine Graphene Region c) Optical Image of the Interface Between Multilayer and Single-Layer GO d) Raman Spectra of a Point in the GO and Pristine Graphene Regions e) Raman Spectra of Different Layers on the Multilayer GO/Single-Layer GO Interface.

Another important feature of Figure 26d can be observed by comparing the G and 2D peaks of the graphene and graphene oxide spectra. In the graphene plot, the 2D peak shows much higher intensity than the G peak, yet in the graphene oxide spectrum, the peaks display roughly the same intensity. However, this disparity is not confined to the specific points analyzed in Figure 26d. Figures 26a and 26b show Raman mapping data over several square micrometers of the graphene oxide and graphene regions, respectively. The Raman mapping software specifically analyzed the ratio of the intensity of the 2D peak to the intensity of the G peak over these areas. Similar to the point-Raman analysis in Figure 26d, the intensity ratio in the graphene oxide region is much lower than in the pristine graphene oxide region. These findings seem to suggest that the pristine region is generally single-layer whereas the graphene oxide region displays characteristics similar to that of bilayer graphene since the 2D/G ratio

generally remains close to unity. However, this phenomenon supports the results of the fluorescence analysis where it was determined that most of the pristine region was in fact single-layer. Also, graphene oxide is essentially a bilayer material, with a graphene underlayer covered by an oxide coating. Therefore, it should be expected that Raman spectroscopy characterizes graphene oxide as a bilayer graphene-like structure. Because this trend is observed both in point-Raman analysis as well as Raman mapping over a significantly large area of the sample, it can be very reasonably concluded that the identification of the pristine graphene and graphene oxide regions from fluorescence microscopy is indeed valid.

The multilayer graphene oxide region on the sample is also investigated in Figures 26c and 26e. Figure 26c displays an optical image of a segment of the interface between the single-layer and multilayer graphene oxide regions. From the image, one can clearly identify the 4 distinct areas of contrast marked by the numbers “1”, “2”, “3”, and “substrate”. Raman spectra were determined for points in each of these regions and tabulated in Figure 26e. Each of the spectra labelled “1”, “2”, and “3” shows characteristics consistent with graphene oxide, whereas the spectrum of the “substrate” region essentially gives a flat line, confirming the presence of bare glass. By comparing the 2D/G ratios of each of the graphene oxide curves reveals the presence single-layer graphene oxide in the region labelled “1”, bilayer graphene oxide in the region labelled “2”, and roughly 3-layer graphene oxide in the region marked “3”. Thus, the Raman data validate the identification of multiple layers of graphene oxide from fluorescence microscopy experiments, demonstrating the viability of FQM as a general characterization technique.

Conclusion

In summary, fluorescence quenching proves to be an effective technique for imaging not only the characteristics of large-area graphene samples, such as the amount and types of defects, sheet uniformity, and the number of layers, but it also demonstrates great sensitivity to the presence of oxidized graphene. In addition to this, FQM displays a high degree of scalability and is thus able to image large-area samples in significantly less time than the more common characterization techniques of Raman spectroscopy, SEM, and TEM. Also unlike most of these techniques, FQM is a nondestructive process which therefore allows the actual samples that are characterized by this method to be used in practical applications. Clearly, then, this study advances the use of macroscale graphene for engineering purposes, such as mechanical support structures or solar cells, by providing a means of characterizing necessarily large quantities of the material. Furthermore, this study supports the practical use of graphene oxide in applications ranging from computer electronics to pharmaceutical medicine by demonstrating the speed and efficiency with which this material can be analyzed by FQM. As fluorescence microscopy continues to expand its usefulness in characterizing graphitic structures, there is great potential for this method to be applied to numerous additional materials.

References

1. Novoselov, K. S.; Geim, A. K.; Morozov, S. V.; Jiang, D.; Zhang, Y.; Dubonos, S. V.; Grigorieva, I. V.; Firsov, A. A. Electric Field Effect in Atomically Thin Carbon Films *Science* **2004** *306* 666-669.
2. Devaney, E. (2011, Oct 7) MIT Discovers that Graphene can Generate Electric Current; Improvements to Night Vision and Solar Energy Systems Could be Next *New England Post*. Retrieved May 27, 2013, from <http://newenglandpost.com>.
3. Savage, N. Materials science: Super carbon *Nature* **2012** *483* S30-S31.
4. Lee, C.; Wei, X.; Kysar, J. W.; Hone, J. Measurement of the Elastic Properties and Intrinsic Strength of Monolayer Graphene *Science* **2008** *321*, 385-388.
5. Geim, A. K.; Novoselov, K. S. The rise of graphene *Nature* **2007** *6* 183-191.
6. Balandin, A. A. Thermal properties of graphene and nanostructured carbon materials *Nature Materials* **2011** *10* 569-581.
7. Duplock, E. J.; Scheffler, M.; Lindan, P. J. D. Hallmark of Perfect Graphene *Phys. Rev. Lett.* **2004** *92* 225502.
8. Cao, Y. C.; Xu, C.; Wu, X.; Wang, X.; Xing, L.; Scott, K. A poly (ethylene oxide)/graphene oxide electrolyte membrane for low temperature polymer fuel cells *Journal of Power Sources* **2011** *196* 8377-8382.
9. Kosynkin, D. V.; Higginbotham, A. L.; Sinitskii, A.; Lomeda, J. R.; Dimiev, A.; Price, B. K.; Tour, J. M. Longitudinal unzipping of carbon nanotubes to form graphene nanoribbons *Nature* **2009** *458* 872-876.
10. Ferrari, A. C.; Basko, D. M. Raman spectroscopy as a versatile tool for studying the properties of graphene *Nature Nanotechnology* **2013** *8* 235-246.
11. Kudin, K. N.; Ozbas, B.; Schniepp, H. C.; Prud'homme, R. K.; Aksay, I. A.; Car, R. Raman Spectra of Graphite Oxide and Functionalized Graphene Sheets *Nanoletters* **2008** *8* 36-41.
12. Retrieved May 27, 2013, from <http://purdue.edu/rem/rs/sem.htm>.
13. Li, X.; Cai, W.; An, J.; Kim, S.; Nah, J.; Yang, D.; Piner, R.; Velamakanni, A.; Jung, I.; Tutuc, E. et al. Large-Area Synthesis of High-Quality and Uniform Graphene Films on Copper Foils *Science* **2009** *324*, 1312-1314.
14. Ding, Y.; Fundamental Theory of Transmission Electron Microscopy. Retrieved May 27, 2013, from <http://nanoscalescience.gatech.edu/zlwang/research/tem.html>.

-
15. Nair, R. R.; Blake, P.; Blake, J. R.; Zan, R.; Anissimova, S.; Bangert, U.; Golovanov, A. P.; Morozov, S. V.; Geim, A. K.; Novoselov, K. S. *et al.* Graphene as a transparent conductive support for studying biological molecules by transmission electron microscopy *Applied Physics Letters* **2010** *97* 153102.
 16. Erickson, K.; Erni, R.; Lee, Z.; Alem, N.; Gannett, W.; Zettl, A. Determination of the Local Chemical Structure of Graphene Oxide and Reduced Graphene Oxide *Advanced Materials* **2010** *22* 4467-4472.
 17. Reina, A.; Jia, X.; Ho, J.; Nezich, D.; Son, H.; Bulovic, V.; Dresselhaus, M. S.; Kong, J. Large Area, Few-Layer Graphene Films on Arbitrary Substrates by Chemical Vapor Deposition *Nano Letters* **2009** *9*, 30-35.
 18. Kim, K. S.; Zhao, Y.; Jang, H.; Lee, Y.; Kim, J. M.; Kim, K. S.; Ahn, J. H.; Kim, P.; Choi, J. Y.; Hong, B. H. Large-scale pattern growth of graphene films for stretchable transparent electrodes *Nature* **2009** *457*, 706-710.
 19. Lee, Y.; Bae, S.; Jang, H.; Jang, S.; Zhu, S. E.; Sim, S. H.; Song, Y. I.; Hong, B. H.; Ahn, J. H. Wafer-Scale Synthesis and Transfer of Graphene Films *Nano Letters* **2010** *10*, 490-493.
 20. Bae, S.; Kim, H.; Lee, Y.; Xu, X.; Park, J. S.; Zheng, Y.; Balakrishnan, J.; Lei, T.; Kim, R.; Song, Y. *et al.* Roll-to-Roll Production of 30-Inch Graphene Films for Transparent Electrodes *Nature Nanotechnology* **2010** *5*, 574-578.
 21. Chae, S. J.; Gunes, F.; Kim, K.; Kim, E. S.; Han, G. H.; Kim, S. M.; Shin, H. J.; Yoon, S. M.; Choi, J. Y.; Park, M. H. *et al.* Synthesis of Large-Area Graphene Layers on Poly-Nickel Substrate by Chemical Vapor Deposition: Wrinkle Formation *Adv. Mat.* **2009** *21*, 2328-2333.
 22. Wang, Y.; Chen, X.; Zhong, Y.; Zhu, F.; Loh, K. P. Large Area, Continuous, Few-Layered Graphene as Anodes In Organic Photovoltaic Devices *Applied Physics Letters* **2009** *95*, 063302-63302-3.
 23. Cooper, C. H.; Zhang, H. F.; Burnin, A.; Bollander, J.C. Carbon Nanotube Yarn, Thread, Rope, Fabric and Composite and Methods of Making the Same *US Patent 0282802* **2009**.
 24. Sun, X.; Liu, Z.; Welsher, K.; Robinson, J. T.; Goodwin, A.; Zaric, S.; Dai, H. Nano-Graphene Oxide for Cellular Imaging and Drug Delivery *Nano Res.* **2008** *1*, 203-212.
 25. Pang, S.; Tsao, H. N.; Feng, X.; Mullen, K. Patterned Graphene Electrodes from Solution-Processed Graphite Oxide Films for Organic Field-Effect Transistors *Adv. Mat.* **2009** *21*, 3488-3491.
 26. Gilje, S.; Han, S.; Wang, M.; Wang, K. L.; Kaner, R. B. A Chemical Route to Graphene for Device Applications *Nano Letters* **2007** *7*, 3394-3398.

-
27. Eda, G.; Fanchini, G.; Chhowalla, M. Large-Area Ultrathin Films of Reduced Graphene Oxide as a Transparent and Flexible Electronic Material *Nature Nanotechnology* **2008** *3*, 270-274.
 28. Robinson, J. T.; Perkins, F. K.; Snow, E. S.; Wei, Z.; Sheehan, P. E. Reduced Graphene Oxide Molecular Sensors *Nano Letters* **2008** *8*, 3137-3140.
 29. Zhou, M.; Zhai, Y.; Dong, S. Electrochemical Sensing and Biosensing Platform Based on Chemically Reduced Graphene Oxide *Anal. Chem.* **2009** *81*, 5603-5613.
 30. Yin, Z.; Wu, S.; Zhou, X.; Huang, X.; Zhang, Q.; Boey, F.; Zhang, H. Electrochemical Deposition of ZnO Nanorods on Transparent Reduced Graphene Oxide Electrodes for Hybrid Solar Cells *Small* **2010** *6*, 307-312.
 31. Rice, G. Microbial Life Educational Resources. Retrieved May 27, 2013, from http://serc.carleton.edu/microbelife/research_methods/microscopy/fluoromic.html
 32. Brasselet, S.; Ferrand, P.; Kress, A.; Wang, X.; Ranchon, H.; Gasecka, A. Imaging Molecular Order in Cell Membranes by Polarization-Resolved Fluorescence Microscopy *Springer Series on Fluorescence* **2013** *13* 311-337.
 33. Walsh, A.; Cook, R. S.; Manning, H. C.; Hicks, D. J.; Lafontant, A.; Arteaga, C. L.; Skala, M. C. Autofluorescence Imaging Resolves Early Cancer Treatment Response In Vivo *The Optical Society* **2013**.
 34. Kaminski, M. T.; Lenzen, S.; Baltrusch, S. Real-time analysis of intracellular glucose and calcium in pancreatic beta cells by fluorescence microscopy *Biochimica et Biophysica Acta (BBA) Molecular Cell Research* **2012** *1823* 1697-1707.
 35. Schneckenburger, H.; Weber, P.; Wagner, M.; Schickinger, S.; Richter, V.; Bruns, T.; Strauss, W. S. L.; Wittig, R. Light exposure and cell viability in fluorescence microscopy *Journal of Microscopy* **2011** *245* 311-318.
 36. Ahn, H. Y.; Fairfull-Smith, K. E.; Morrow, B. J.; Lussini, V.; Kim, B.; Bondar, M. V.; Bottle, S. E.; Belfield, K. D. Two-Photon Fluorescence Microscopy Imaging of Cellular Oxidative Stress Using Profluorescent Nitroxides *Journal of the American Chemical Society* **2012** *134* 4721-4730.
 37. Lipman, T.; Tabakman, R.; Lazarovici, P. Neuroprotective effects of the stable nitroxide compound Tempol on 1-methyl-4-phenylpyridinium ion-induced neurotoxicity in the nerve growth factor-differentiated model of pheochromocytoma PC12 cells *Eur. J. Pharmacol.* **2006** *549* 50-57.
 38. Raju, S. V. Y.; Barouch, L. A.; Hare, J. M. Nitric Oxide and Oxidative Stress in Cardiovascular Aging *Sci. Aging Knowl. Environ.* **2005** *2005* 1-7.

-
39. Varadarajan, S.; Yatin, S.; Aksenova, M.; Butterfield, D. A. Review: Alzheimer's amyloid beta-peptide-associated free radical oxidative stress and neurotoxicity. *J. Struct. Biol.* **2000** *130* 184-208.
40. Kyle, J. R.; Guvenc, A.; Wang, W.; Ghazinejad, M.; Lin, J.; Guo, S.; Ozkan, C. S.; Ozkan, M. Centimeter-Scale High Resolution Metrology of Entire CVD-Grown Graphene Sheets *Small* **2011** *7*, 2599-2606.
41. Ghazinejad, M.; Kyle, J. R.; Guo, S.; Pleskot, D.; Bao, D.; Vullev, V. I.; Ozkan, M.; Ozkan, C. S. Non-Invasive High-Throughput Metrology of Functionalized Graphene Sheets *Adv. Functional Mat.* **2012** *22*, 4519-4525.
42. Dong, H.; Gao, W.; Yan, F.; Ji, H.; Ju, H. Fluorescence Resonance Energy Transfer between Quantum Dots and Graphene Oxide for Sensing Biomolecules *Anal. Chem.* **2010** *82*, 5511-5517.
43. Cao, L.; Cheng, L.; Zhang, Z.; Wang, Y.; Zhang, X.; Chen, H.; Liu, B.; Zhang, S.; Kong, J. Visual and high-throughput detection of cancer cells using a graphene oxide-based FRET aptasensing microfluidic chip *Lab on a Chip* **2012** *12*, 4864-4869.
44. Zhu, Z.; Yang, R. H.; You, M. X.; Zhang, X. L.; Wu, Y. R.; Hong, W. Single-Walled Carbon Nanotube as an Effective Quencher *Anal. Bioanal. Chem.* **2010** *396*, 73-83.
45. Liu, Y.; Liu, C. Y.; Liu, Y. Investigation on Fluorescence Quenching of Dyes by Graphite Oxide and Graphene *Applied Surface Science* **2011** *257*, 5513-5518.
46. Nguyen, H. B.; Nguyen, V. C.; Nguyen, V. T.; Ngo, T. T. T.; Nguyen, N. T.; Dang, T. T. H.; Tran, D. L.; Do, P. Q.; Nguyen, X. N.; Nguyen, X. P. Graphene patterned polyaniline-based biosensor for glucose detection *Advances in Natural Science: Nanoscience and Nanotechnology* **2012** *3* 025011.

Appendix: Image Processing Software

Generating the reference image from a pristine glass slide:

```
%% %%%%%%%%%%%%%%%%%%%%%%%%%%%%%%%%%%%%%%%%%%%%%%%%%%%%%%%%%%%%%%%%%%%%%%%%%
%%% Created by: Jennifer Reiber Kyle in 2011
%%% Nanotechnology and Biomedical Science Laboratory
%%% e-mail: jennifer.reiberkyle@gmail.com
%%%
%%% For: CEPCEB at UCR - Dr. Carter, thanks for all your help!
%% %%%%%%%%%%%%%%%%%%%%%%%%%%%%%%%%%%%%%%%%%%%%%%%%%%%%%%%%%%%%%%%%%%%%%%%%%

%% USER PARAMETERS
%% %%%%%%%%%%%%%%%%%%%%%%%%%%%%%%%%%%%%%%%%%%%%%%%%%%%%%%%%%%%%%%%%%%%%%%%%%

% Image Settings
% nondefault_image_width = 1344; % default value: 1344
% nondefault_image_height = 1024; % default value: 1024

%% %%%%%%%%%%%%%%%%%%%%%%%%%%%%%%%%%%%%%%%%%%%%%%%%%%%%%%%%%%%%%%%%%%%%%%%%%
%%

%% DO NOT ALTER BELOW THESE LINES
%% %%%%%%%%%%%%%%%%%%%%%%%%%%%%%%%%%%%%%%%%%%%%%%%%%%%%%%%%%%%%%%%%%%%%%%%%%
if(exist('nondefault_image_width','var')),
nondefault_values{'nondefault_image_width'} =
nondefault_image_width; end
if(exist('nondefault_image_height','var')),
nondefault_values{'nondefault_image_height'} =
nondefault_image_height; end

addpath 'scripts/';
if exist('nondefault_values','var')
    ReiberKyle_makeBackgroundScript(nondefault_values);
else
    ReiberKyle_makeBackgroundScript();
end
```

Code for 'makeBackgroundScript':

```
%% %%%%%%%%%%%%%%%%%%%%%%%%%%%%%%%%%%%%%%%%%%%%%%%%%%%%%%%%%%%%%%%%%%%%%%%%%
%%% Created by: Jennifer Reiber Kyle in 2011
%%% Nanotechnology and Biomedical Science Laboratory
%%% e-mail: jennifer.reiberkyle@gmail.com
%%%
%%% For: CEPCEB at UCR - Dr. Carter, thanks for all your help!
%% %%%%%%%%%%%%%%%%%%%%%%%%%%%%%%%%%%%%%%%%%%%%%%%%%%%%%%%%%%%%%%%%%%%%%%%%%
function [ReturnPathName] =
ReiberKyle_makeBackgroundScript(nondefault_values)
close all;
```



```

%% default settings
global RootDir SaveDir;
RootDir = 'ImageFolder/';
SaveDir = 'OutputFolder/';

global MAXINTENSITY NUMBEROFHISTOGRAMSTEPS;
MAXINTENSITY = 2^12;
NUMBEROFHISTOGRAMSTEPS = 2^16/4;
%% End: default settings

%% Image Specs
global owidth oheight mSize;
if(exist('nondefault_values{nondefault_image_width}','var'))
    owidth = nondefault_image_width;
else
    owidth = 1344;
end
if(exist('nondefault_values{nondefault_image_height}','var'))
    oheight = nondefault_image_height;
else
    oheight = 1024;
end
mSize = 4; %downsample size for small montage representation
%% End: Image Specs

%% Algorithm
% Get image to process
[OrigFileName,OrigPathName] = uigetfile('*.tif*', 'Select image to
breakdown...', RootDir, 'MultiSelect', 'off');
if(~OrigFileName)
    return
end

% Get Binning settings
[s,v] = listdlg('PromptString','Select bin number:',...
    'SelectionMode','single',...
    'ListSize',[100,60],...
    'ListString',{'B1','B2','B4','B8'});
BinNumber = 2^(s-1);

ImagePathName =
ReiberKyle_breakdown(OrigFileName,OrigPathName,1,BinNumber);

figure('Name', 'Original: IMG (col)x(row)')
imshow(imread([ImagePathName 'smallMontageOriginal.tif']));

files = dir(fullfile(ImagePathName,'IMG*.mat*'));

%%Select Images
[s,v] = listdlg('Name','Select images:',...
    'PromptString','IMG (column)x(row)',...

```

```

        'SelectionMode','multiple',...
        'ListSize',[150,700],...
        'ListString',{files.name});
ImageFileName = {files(s).name};
numberOfFiles = length(ImageFileName);

%%Load Matrices
load([ImagePathName ImageFileName{1,1}]);
newImageFile = double(data);
for i=2:length(ImageFileName)
    load([ImagePathName ImageFileName{1,i}]);
    newImageFile = newImageFile+data;
end

disp('Compiling selected pieces into background image');
newImageFile = int16(newImageFile/length(ImageFileName));
figure('Name', 'Average')
imshow(mat2gray(newImageFile));

backgroundFileName = [SaveDir 'Background-' OrigFileName];
if(exist(backgroundFileName) == 2)
    i = 1;
    while 1
        backgroundFileName = [SaveDir 'Background-'
strtok(OrigFileName, '.') '-' num2str(i) '.tif'];
        if (exist(backgroundFileName) ~= 2)
            break
        else
            i = i+1;
        end
    end
end
end

imwrite(uint16(newImageFile), backgroundFileName, 'compression',
'none');
rmdir(ImagePathName,'s');

return;

```

Generating the flattened montage image:

```

%% %%%%%%%%%%%
%%% Created by: Jennifer Reiber Kyle in 2011
%%% Nanotechnology and Biomedical Science Laboratory
%%% e-mail: jennifer.reiberkyle@gmail.com
%%%
%%% For: CEPCEB at UCR - Dr. Carter, thanks for all your help!
%% %%%%%%%%%%%

%% USER PARAMETERS

```

```

%%%%%%%%%%%%%%%%%%%%%%%%%%%%%%%%%%%%%%%%%%%%%%%%%%%%%%%%%%%%%%%%%%%%%%%%
% Image Settings
%nondefault_image_width = 1344; % default value: 1344
%nondefault_image_height = 1024; % default value: 1024

%%%%%%%%%%%%%%%%%%%%%%%%%%%%%%%%%%%%%%%%%%%%%%%%%%%%%%%%%%%%%%%%%%%%%%%%
%%
%% DO NOT ALTER BELOW THESE LINES
%%%%%%%%%%%%%%%%%%%%%%%%%%%%%%%%%%%%%%%%%%%%%%%%%%%%%%%%%%%%%%%%%%%%%%%%

if(exist('nondefault_image_width','var')),
nondefault_values{'nondefault_image_width'} =
nondefault_image_width; end
if(exist('nondefault_image_height','var')),
nondefault_values{'nondefault_image_height'} =
nondefault_image_height; end

addpath 'scripts/';
if exist('nondefault_values','var')
    ReiberKyle_flattenMontageScript(nondefault_values);
else
    ReiberKyle_flattenMontageScript();
end

```

Code for 'flattenMontageScript':

```

%% %%%%%%%%%%%
%%% Created by: Jennifer Reiber Kyle in 2011
%%% Nanotechnology and Biomedical Science Laboratory
%%% e-mail: jennifer.reiberkyle@gmail.com
%%%
%%% For: CEPCEB at UCR - Dr. Carter, thanks for all your help!
%% %%%%%%%%%%%
function [ReturnPathName] =
ReiberKyle_flattenMontageScript(nondefault_values)

%% default settings
global RootDir SaveDir;
RootDir = 'ImageFolder/';
SaveDir = 'OutputFolder/';

global MAXINTENSITY NUMBEROFHISTOGRAMSTEPS;
MAXINTENSITY = 2^12;
NUMBEROFHISTOGRAMSTEPS = 2^16/4;
%% End: default settings

```

```

%% Image Specs
global owidth oheight mSize;
if(exist('nondefault_values{nondefault_image_width}','var'))
    owidth = nondefault_values(nondefault_image_width);
else
    owidth = 1344;
end
if(exist('nondefault_values{nondefault_image_height}','var'))
    oheight = nondefault_values(nondefault_image_height);
else
    oheight = 1024;
end
mSize = 4; %downsample size for small montage representation
%% End: Image Specs

%% Algorithm
% Get image(s) to process
[ImageFileName,ImagePathName] = uigetfile('*.tif*', 'Select image(s)
to breakdown...', RootDir, 'MultiSelect', 'on');
if(~ImageFileName)
    return
end
if(class(ImageFileName) == 'cell') %multiple files
    numberOfFiles = length(ImageFileName);
elseif(class(ImageFileName) == 'char') %single file
    tempF = ImageFileName; clear ImageFileName;
    ImageFileName = {tempF};
    numberOfFiles = 1;
end

% Get Binning settings
[s,v] = listdlg('PromptString','Select bin number:',...
    'SelectionMode','single',...
    'ListSize',[100,60],...
    'ListString',{'B1','B2','B4','B8'});
BinNumber = 2^(s-1);

% Get background image
[RefFileName,RefPathName] = uigetfile('*.tif*', 'MultiSelect',
'off', 'Select Background Image...', RootDir);
if(~RefFileName)
    return
end

if(numberOfFiles > 1)
    SkipEval = 1;
    Method = 'Basic';
else
    SkipEval = 0;
    Method = questdlg('Choose Correction Method', ...
        'Background Correction:', ...

```

```

        'Basic','Manual Correct', 'Basic');
end

if(BinNumber > 2)
    SkipBin = questdlg('Original image binned. Adjust reference
image for binning?', ...
        'Reference Image Adjustment:', ...
        'Bin','Skip', 'Skip');
else
    SkipBin = 'Skip';
end

ReturnPathName = 'blank'
for i=1:numberOfFiles
    close all
    [tempPath] =
ReiberKyle_breakdown(ImageFileName{1,i},ImagePathName,1,BinNumber);
    newImagePathName(1,i) = {tempPath};
    if(1 == i)
        ReturnPathName = newImagePathName(1,i)
    end
    %disp(['New Folder: ' newImagePathName{1,i}]);

ReiberKyle_flatten(newImagePathName{1,i},RefFileName,RefPathName,1,M
method,SkipEval, SkipBin);
    ReiberKyle_rebuild(newImagePathName{1,i},1,1);
end
disp('Flattening completed')
return

```

Code for 'flatten':

```

%% %%%%%%%%%%%
%% Created by: Jennifer Reiber Kyle in 2011
%% Nanotechnology and Biomedical Science Laboratory
%% e-mail: jennifer.reiberkyle@gmail.com
%%
%% For: CEPCEB at UCR - Dr. Carter, thanks for all your help!
%% %%%%%%%%%%%
function [] =
ReiberKyle_flatten(newImagePathName,RefFileName,RefPathName,highdef,
Method,SkipEval, SkipBin)

global owidth oheight mSize;

%Default values
if(~exist('SkipEval','var'))
    SkipEval = 0;
end

```

```

if(~exist('highdef','var'))
    highdef = 1;
end

%% Load original image
if(~exist('newImagePathName','var'))
    newImagePathName = [uigetdir(SaveDir, 'Original Image
Directory') '\\'];
end

load([newImagePathName 'originalImageFileData.mat'], 'bnum');
load([newImagePathName 'smallMontageOriginal.mat']);
smallMontage = data; clear data;
%figure('Name', 'Original Montage'),imshow(mat2gray(smallMontage));

%% Load/bin ref image
if(~exist('RefFileName','var'))
    [RefFileName,RefPathName] = uigetfile('*.tif*', 'MultiSelect',
'off', 'Select Background Image...', RootDir);
end
if(~RefFileName)
    return
end
if(bnum > 1)
    if(~exist('SkipBin','var'))
        SkipBin = questdlg('Original image binned. Adjust reference
image for binning?', ...
        'Reference Image Adjustment:', ...
        'Bin','Skip', 'Skip');
    end

    switch SkipBin
        case 'Bin'
            ref = binImage(double(imread([RefPathName
RefFileName])),bnum);
        case 'Skip'
            ref = double(imread([RefPathName RefFileName]));
    end
else
    ref = double(imread([RefPathName RefFileName]));
end

%% Create smallrefmontage
[rheight rwidth] = size(ref);
load([newImagePathName 'originalImageFileData.mat'],
'ImageFileName', 'imheight', 'imwidth', 'bnum');
load([newImagePathName 'smallMontageFileData.mat'], 'mwidth',
'mheight', 'DownSampleStep', 'sdheight', 'sdwidth');

```

```

%data =
double(originalImageFile(1:DownSampleStep:imheight,1:DownSampleStep:
imwidth));

sref = ref(1:DownSampleStep:rheight,1:DownSampleStep:rwidth); clear
rheight rwidth;

[srheight srwidth] = size(sref);
if((srheight ~= sdheight) || (srwidth ~= sdwidth))
    disp('Reference image dimensions do not match original image
dimensions, cancelling flatten procedure.');
```

return

```
end

% Build up reference small montage
r2 = ones(size(smallMontage));%[srheight*mheight srwidth*mwidth]);
for mx=1:mwidth
    for my = 1:mheight
        o_srheight = (my-1)*srheight;
        o_srwidth = (mx-1)*srwidth;

        r2(
(1+o_srheight):(srheight+o_srheight), (1+o_srwidth):(srwidth+o_srwidt
h) ) = sref;
        end
    end
end
clear sref data;

%% Background Correct
tryagain = 1;
while tryagain
    if(exist('Method'))
        choice = Method;
    else
        if(highdef)
            choice = questdlg('Choose Correction Method', ...
                'Background Correction:', ...
                'Basic','Manual Correct', 'Basic');
```

else

```
            choice = questdlg('Choose Correction Method', ...
                'Background Correction:', ...
                'Basic','Manual Correct', 'Basic');
```

end

```
        end
    end
    switch choice
        case 'Manual Correct'
            ref_offset = ReiberKyle_manualFlatten(smallMontage,r2);
            ref = ref+ref_offset;
            r2 = r2+ref_offset;
        case 'Optimized'
```

```

        [EvalFileName,EvalPathName] = uigetfile('IMG*.mat*',
'Select image', newImagePathName, 'MultiSelect', 'off');
        load([EvalPathName EvalFileName]);
        eval = double(data); clear data;
        figure('Name','Original Image'), imagesc(eval);
        figure('Name','Reference Image'), imagesc(ref);

        evaloffset = log10(eval);
        lightClearedImage = 10.^(evaloffset - log10(ref) +
log10(mean(mean(ref))));
        ecorr = corr2(lightClearedImage,ref)
        figure('Name','Simple Background Removal')
        imagesc(lightClearedImage);

        offset = min(min(ref))/2;

        %Check if addition decreases correlation
        ref2 = ref + offset*ones(size(ref));
        lightClearedImage = 10.^(evaloffset - log10(ref2) +
log10(mean(mean(ref2))));
        pluscorr = corr2(lightClearedImage,ref2);

        ref2 = ref - offset*ones(size(ref));
        lightClearedImage = 10.^(evaloffset - log10(ref2) +
log10(mean(mean(ref2))));
        minuscorr = corr2(lightClearedImage,ref2);

        ittno = 12;
        if ((abs(ecorr) < abs(minuscorr)) && (abs(ecorr) <
abs(pluscorr)))
            disp('Original value decreases correlation');
            [ref,ecorr,imoffset,offnumber] =
backgroundOptimize(ref,eval,offset,ittno);
        elseif (abs(minuscorr) < abs(pluscorr))
            disp('Subtraction decreases correlation');

            ref = ref - offset;
            [ref,ecorr,imoffset,offnumber] =
backgroundOptimize(ref,eval,offset,ittno);
            imoffset = imoffset - offset;
        else
            disp('Addition decreases correlation');

            ref = ref + offset;

            [ref2,ecorr,imoffset,offnumber] =
backgroundOptimize(ref,eval,offset,1);
            maxoffset = (2^16 - max(max(ref)))/2;
            while (offnumber == 1)
                disp('Hit addition maximum limit, increasing
offset range');

```



```

        offset = offset * 2;
        ittno = ittno + 1;
        if(offset > maxoffset)
            disp('Error with optimization, went over
maximum range. Using maximum range.');
```

maximum range. Using maximum range.');

```

            offset = maxoffset;
            break;
        end
        ref = ref + offset;
        [ref2,ecorr,imoffset,offnumber] =
backgroundOptimize(ref,eval,offset,1);
        end
        [ref,ecorr,imoffset,offnumber] =
backgroundOptimize(ref,eval,offset,ittno);
        imoffset = imoffset + offset;
    end
    lightClearedImage = 10.^(evaloffset - log10(ref) +
log10(mean(mean(ref))));
    ecorr = corr2(lightClearedImage,ref)
    imoffset;
    figure('Name','Optimized Background Removal')
    imagesc(lightClearedImage);
end

    smallMontageFlat = 10.^(log10(double(smallMontage)) - log10(r2)
+ log10(mean(mean(r2))));

    figure('Name', [ImageFileName ' -
Flattened']),imshow(mat2gray(smallMontageFlat));
    if(SkipEval)
        choice = 'Accept';
    else
        pause(5)

        choice = questdlg('Evaluate Background Correction', ...
'Background Correction:', ...
'Accept','Try Again','Cancel', 'Accept');
end
switch choice
case 'Try Again'
    clear Method;
case 'Cancel'
    tryagain = 0;
case 'Accept'
    tryagain = 0;

    %Save Flattened Montage
    data = smallMontageFlat;
    save([newImagePathName 'smallMontageFlat.mat'], 'data');
    imwrite(uint8(2^8*data/max(max(data))),
[newImagePathName 'smallMontageFlat.tif'], 'Compression', 'none');
```

```

clear data r2 sref srheight srwidth;

%Apply Backgrounding
refoffset = - log10(double(ref)) +
log10(mean(mean(ref)));
files = dir([newImagePathName 'IMG*.mat']);
numberOfFiles = length(files);
for fileIndex = 1:numberOfFiles
    fileName = files(fileIndex).name;
    load([newImagePathName fileName]);
    data = 10.^(log10(data) + refoffset);
    save([newImagePathName fileName], 'data');
end
clear refoffset files numberOfFiles fileName data;

end
end

```

Code for 'breakdown':

```

%% %%%%%%%%%%%
%%% Created by: Jennifer Reiber Kyle in 2011
%%% Nanotechnology and Biomedical Science Laboratory
%%% e-mail: jennifer.reiberkyle@gmail.com
%%%
%%% For: CEPCEB at UCR - Dr. Carter, thanks for all your help!
%% %%%%%%%%%%%
function [newImagePathName] =
ReiberKyle_breakdown(ImageFileName, ImagePathName, highdef, BinNumber)

global owidth oheight mSize;
global SaveDir;
global MAXINTENSITY NUMBEROFHISTOGRAMSTEPS;

if(exist('BinNumber', 'var'))
    bnum = BinNumber;
else
    [s,v] = listdlg('PromptString','Select bin number:',...
        'SelectionMode','single',...
        'ListSize',[100,60],...
        'ListString',{'B1','B2','B4','B8'});
    bnum = 2^(s-1);
end

originalImageFile = imread([ImagePathName ImageFileName]);

%BreakDown Folder
%%%%
%disp('Creating Folder');
i = 1;

```

```

while 1
    newImagePathName = [SaveDir strtok(ImageFileName, '.') '-V'
num2str(i) '/'];
    if (~isdir(newImagePathName))
        mkdir(newImagePathName);
        break
    else
        i = i+1;
    end
end

% Get/Store original image dimensions
[imheight imwidth] = size(originalImageFile);
save([newImagePathName 'originalImageFileData.mat'],
'ImageFileName', 'imheight', 'imwidth', 'bnum');

% Get montage tile dimensions
iwidth = owidth/bnum; iheight = oheight/bnum;
mwidth = imwidth/iwidth; mheight = imheight/iheight;

% if(highdef)disp('Saving Pieces');for mx=1:mwidthfor my = 1:mheight
%     data = double(originalImageFile((1+(my-
1)*iheight):(iheight+(my-1)*iheight), (1+(mx-1)*iwidth):(iwidth+(mx-
1)*iwidth)));
%     save([newImagePathName 'IMG' num2str(mx) 'x'
num2str(my) '.mat'], 'data');
%     end end end clear data
%disp('Creating low-def image');
% oImgFileSize = size(originalImageFile);

% Determine downsampled image dimensions, use them to create small
montage
% template
DownSampleStep =
2^round(log2(sqrt(imheight*imwidth/(iwidth*iheight*mSize))));
sdheight = ceil(iheight/DownSampleStep); sdwidth =
ceil(iwidth/DownSampleStep);
% sdata = ones(1:DownSampleStep:iheight,1:DownSampleStep:iwidth);
% [sdheight sdwidth] = size(sdata);
dataSM = ones([sdheight*mheight sdwidth*mwidth]);

% Store downsample dimensions
save([newImagePathName 'smallMontageFileData.mat'], 'mwidth',
'mheight', 'DownSampleStep', 'sdheight', 'sdwidth');

% sref = ref(1:DownSampleStep:rheight,1:DownSampleStep:rwidth);
% r2((1+(my-1)*srheight):(srheight+(my-1)*srheight), (1+(mx-
1)*srwidth):(srwidth+(mx-1)*srwidth)) = sref;
disp('Storing montage for processing');

```

```

if(highdef)
    disp('...and saving Pieces');
end

for mx=1:mwidth
    for my = 1:mheight
        % Pull out appropriate tile
        o_iheight = (my-1)*iheight;
        o_iwidth = (mx-1)*iwidth;
        data = double(originalImageFile(
(1+o_iheight):(iheight+o_iheight), (1+o_iwidth):(iwidth+o_iwidth) ));

        % Save tile if in highdef mode
        if(highdef)
            save([newImagePathName 'IMG' num2str(mx) 'x' num2str(my)
'.mat'], 'data');
        end

        % Downsample tile
        sdata =
data(1:DownSampleStep:iheight,1:DownSampleStep:iwidth);

        % Store downsampled tile in small montage
        o_sdheight = (my-1)*sdheight;
        o_sdwidth = (mx-1)*sdwidth;
        dataSM(
(1+o_sdheight):(sdheight+o_sdheight), (1+o_sdwidth):(sdwidth+o_sdwidth)
) = sdata;
        end
    end
end

%data =
%double(originalImageFile(1:DownSampleStep:imheight,1:DownSampleStep
:imwidth));
%datasize = size(data)

% Store small montage as a matlab file
clear data;
data = dataSM;
save([newImagePathName 'smallMontageOriginal.mat'], 'data');

% Store small montage as a tif image
imwrite(uint8(2^8*data/max(max(data))), [newImagePathName
'smallMontageOriginal.tif'], 'Compression', 'none');
figure('Name', [ImageFileName ' -
Original']), imshow(mat2gray(data));

end

```

Code for 'rebuild':

```
%% %%%%%%%%%%%  
%%% Created by: Jennifer Reiber Kyle in 2011  
%%% Nanotechnology and Biomedical Science Laboratory  
%%% e-mail: jennifer.reiberkyle@gmail.com  
%%%  
%%% For: CEPCEB at UCR - Dr. Carter, thanks for all your help!  
%% %%%%%%%%%%%  
function [newSaveFileName] =  
ReiberKyle_rebuild(ImagePathName,highdef,clearfolder,loadImageFileNa  
me)  
  
global SaveDir;  
global owidth oheight;  
  
if(~exist('ImagePathName','var')) % Default values  
    ImagePathName = [uigetdir(SaveDir, 'Image Directory') '\'];  
end  
if(~exist('highdef','var'))  
    highdef = 1;  
end  
if(~exist('clearfolder','var'))  
    clearfolder = 0;  
end  
  
if(~exist('loadImageFileName','var'))  
    loadImageFileName = 'smallMontageFlat.mat';  
    if(~exist([ImagePathName loadImageFileName],'file'))  
        loadImageFileName = 'smallMontageOriginal.mat';  
        if(~exist([ImagePathName loadImageFileName],'file'))  
            disp('No montage file found to rebuild');  
            return;  
        end  
    end  
end  
end  
  
%%Open/Select Montage Image  
load([ImagePathName loadImageFileName]);  
smallImage = data; clear data;  
  
if(highdef)  
    files = dir([ImagePathName 'IMG*.mat']);  
    numberOfFiles = length(files);  
  
    load([ImagePathName 'originalImageFileData.mat'],  
'ImageFileName', 'imheight', 'imwidth', 'bnum');  
    iwidth = owidth/bnum; iheight = oheight/bnum;
```

```

montageImage = uint16(ones(imheight,imwidth));
for fileIndex = 1:numberOfFiles
    fileName = files(fileIndex).name;
    load ([ImagePathName fileName]);
    fileName = strtok(fileName, 'IMG');
    [xstr fileName] = strtok(fileName, 'x');
    ystr = strtok(fileName(2:length(fileName)), '.mat');
    mx = str2num(xstr);
    my = str2num(ystr);
    montageImage((1+(my-1)*iheight):(iheight+(my-
1)*iheight), (1+(mx-1)*iwidth):(iwidth+(mx-1)*iwidth)) =
uint16(data);
    end
    clear data;
end

rebuiltFileName = [SaveDir 'Flattened-' ImageFileName];
smallFileName = [SaveDir 'Flattened-' strtok(ImageFileName, '.') '-
small.tif'];
if((exist(rebuiltFileName) == 2) || (exist(smallFileName) == 2))
    i = 1;
    while 1
        rebuiltFileName = [SaveDir 'Flattened-'
strtok(ImageFileName, '.') '-' num2str(i) '.tif'];
        smallFileName = [SaveDir 'Flattened-' strtok(ImageFileName,
'.') '-' num2str(i) '-small.tif'];
        if ((exist(rebuiltFileName) ~= 2) && (exist(smallFileName)
~= 2))
            break
        else
            i = i+1;
        end
    end
end

imwrite(uint16(montageImage), rebuiltFileName, 'compression',
'none');
imwrite(uint8(2^8*smallImage/max(max(smallImage))), smallFileName,
'Compression', 'none');
if(clearfolder)
    rmdir(ImagePathName, 's');
end
return

```

Generating flattened images manually:

```

function [ref_offset] = manualFlatten(original,ref)

if(~exist('original'))

```

```

    Rootdir = 'C:\JenData\ImageProc\ProcImages\2011_03_08_-
flattened-small\';
    [ImageFileName,ImagePathName] = uigetfile('*.tif*', 'Select
image to flatten...',Rootdir);
    original = imread([ImagePathName ImageFileName]);
    [RefFileName,RefPathName] = uigetfile('*.tif*', 'Select
reference image...',Rootdir);
    ref = imread([RefPathName RefFileName]);
end

%% Downsample images
maxDim = [400, 400];
osize = size(original);
multV = osize./maxDim;
DownSampleStep = max([floor(min(multV)) 1]);
[oheight owidth] = size(original);
o2 = original(1:DownSampleStep:oheight,1:DownSampleStep:owidth);
r2 = ref(1:DownSampleStep:oheight,1:DownSampleStep:owidth);

%f = figure('Visible','off','Toolbar',
'figure','Position',[360,500,450,285]);
f = figure('Visible','off','Toolbar',
'figure','Position',[360,500,700,450]);

ff_offset = 0;
f_offset = 0;
c_offset = 0;
ref_offset = 0;
htext = uicontrol('Style','text','String','Reference Offset',...
'Position',[705,250,100,15]);
% 'Position',[305,250,100,15]);

hnum = uicontrol('Style','edit',...
'String',num2str(ref_offset),...
'Position',[715,220,70,25],...
'Callback',{@edittext1_Callback});
% 'Position',[315,220,70,25],...

hcontinue = uicontrol('String','Return to Image Flattening',...
'Position',[395,140,140,25],...
'Callback','uiresume(gcbf)');
% 'Position',[295,140,140,25],...

cslideMin = -10000; cslideMax = 10000;
fslideMin = -1000; fslideMax = 1000;
ffslideMin = -100; ffslideMax = 100;
hffslider =
uicontrol('Style','slider','Min',ffslideMin,'Max',ffslideMax,...
'Value',0,'SliderStep',[0.05 0.6],...
'Position',[55,30,20,400],...

```

```

        'Callback',{@ffslider1_Callback})

hfslider =
uicontrol('Style','slider','Min',fslideMin,'Max',fslideMax,...
        'Value',0,'SliderStep',[0.05 0.6],...
        'Position',[30,30,20,400],...
        'Callback',{@fslider1_Callback})

hcslider =
uicontrol('Style','slider','Min',cslideMin,'Max',cslideMax,...
        'Value',0,'SliderStep',[0.05 0.6],...
        'Position',[5,30,20,400],...
        'Callback',{@cslider1_Callback})

ha = axes('Units','pixels','Position',[50,30,400,400]);
%ha = axes('Units','pixels','Position',[50,60,200,185]);
align([htext,hnum,hcontinue],'Center','None');

%set([f,hsurf,hmesh,hcontour,htext,hpopup],...
set([f,htext,hnum,hcontinue],...
    'Units','normalized');

flat = 10.^(log10(double(o2)) - log10(r2) + log10(mean(mean(r2))));
imshow(mat2gray(flat));
set(f,'Name','Flatten Image')
movegui(f,'center')

set(f,'Visible','on')

% Push button callbacks. Each callback plots current_data in
% the specified plot type.
function edittext1_Callback(hObject, eventdata, handles)
    user_entry = str2double(get(hObject,'string'))
    if isnan(user_entry)
        errordlg('You must enter a numeric value','Bad
Input','modal')
        uicontrol(hObject)
        return
    end
end

function ffslider1_Callback(hObject, eventdata, handles)
    ff_offset = get(hObject,'Value');
    ref_offset = ff_offset + f_offset + c_offset;
    r3 = r2 + ref_offset;
    set(hnum,'String',num2str(ref_offset));
    flat = 10.^(log10(double(o2)) - log10(r3) +
log10(mean(mean(r3))));
    imshow(mat2gray(flat));
end

```



```

function fslider1_Callback(hObject, eventdata, handles)
    f_offset = get(hObject, 'Value');
    ref_offset = ff_offset + f_offset + c_offset;
    r3 = r2 + ref_offset;
    set(hnum, 'String', num2str(ref_offset));
    flat = 10.^(log10(double(o2)) - log10(r3) +
log10(mean(mean(r3))));
    imshow(mat2gray(flat));
end

function cslider1_Callback(hObject, eventdata, handles)
    c_offset = get(hObject, 'Value');
    ref_offset = ff_offset + f_offset + c_offset;
    r3 = r2 + ref_offset;
    set(hnum, 'String', num2str(ref_offset));
    flat = 10.^(log10(double(o2)) - log10(r3) +
log10(mean(mean(r3))));
    imshow(mat2gray(flat));
end

uiwait(gcf);
close(f)
end

```

Adjusting intensity values:

```

%% %%%%%%%%%%%
%%% Created by: Jennifer Reiber Kyle in 2011
%%% Nanotechnology and Biomedical Science Laboratory
%%% e-mail: jennifer.reiberkyle@gmail.com
%%%
%%% For: CEPCEB at UCR - Dr. Carter, thanks for all your help!
%% %%%%%%%%%%%
%% DO NOT ALTER BELOW THESE LINES
%%%%%%%%%%%%
addpath 'scripts/';
ReiberKyle_adjustIntensityScript();

```

Code for 'adjustIntensityScript':

```

%% %%%%%%%%%%%
%%% Created by: Jennifer Reiber Kyle in 2011
%%% Nanotechnology and Biomedical Science Laboratory
%%% e-mail: jennifer.reiberkyle@gmail.com
%%%
%%% For: CEPCEB at UCR - Dr. Carter, thanks for all your help!
%% %%%%%%%%%%%
function [] = adjustIntensityScript()

```

```

%% default settings
global RootDir SaveDir;
RootDir = 'ImageFolder/';
SaveDir = 'OutputFolder/';

%% Get image(s) to process
[ImageFileName,ImagePathName] = uigetfile('*.tif*', 'Select 12bit
image(s) to adjust intensity...', RootDir, 'MultiSelect', 'on');
if(~ImageFileName)
    return
end
if(class(ImageFileName) == 'cell') %multiple files
    numberOfFiles = length(ImageFileName);
elseif(class(ImageFileName) == 'char') %single file
    tempF = ImageFileName; clear ImageFileName;
    ImageFileName = {tempF};
    numberOfFiles = 1;
end

Method = questdlg('Choose desired bit depth', ...
    'Adjust Intensity:', ...
    '8bit','16bit', '16bit');

for i=1:numberOfFiles
    close all
    img = imread([ImagePathName ImageFileName{1,i}]);

    adjustedFileName = [SaveDir 'Adjusted-' Method '-'
ImageFileName{1,i}];
    if(exist(adjustedFileName) == 2)
        i = 1;
        while 1
            adjustedFileName = [SaveDir 'Adjusted-' Method '-'
strtok(ImageFileName{1,i}, '.') '-' num2str(i) '.tif'];
            if (exist(adjustedFileName) ~= 2)
                break
            else
                i = i+1;
            end
        end
    end
end

switch Method
case '8bit'
    img = uint8(img/(2^4));
    imwrite(img, adjustedFileName, 'Compression', 'none');
case '16bit'
    img = img*(2^4);
    imwrite(img, adjustedFileName, 'Compression', 'none');
end
end
end

```